# Experimentally-derived F, Cl and Br fluid/melt partitioning of intermediate to silicic melts in shallow magmatic systems

*Cassidy, Mike,[1*] Iveson, Alex A,[2] Humphreys, Madeleine, C.S,[2] Mather, Tamsin A.,[1] Helo, Christoph.,[3] Castro, Jonathan M.,[3] Ruprecht, Philipp[4], Pyle, David M.,[1] EIMF[5]*

[1]Department of Earth Sciences, University of Oxford, UK

[2]Department of Earth Science, University of Durham, UK

[3]Institute for Geoscience, Johannes Gutenberg University of Mainz, Germany

[4]Department of Geological Sciences and Engineering, University of Nevada, Reno, USA

[5]Edinburgh Ion Microprobe Facility, UK

*Corresponding author: michael.cassidy@earth.ox.ac.uk*

## ABSTRACT

The conditions under which halogens partition in favour of an exsolved fluid relative to the coexisting melt are key for understanding many magmatic processes, including volcanic degassing, evolution of crustal melt bodies, and ore formation. We report new F, Cl and Br fluid/melt partition coefficients for intermediate to silicic melts, for which F and Br data are particularly lacking; and for varying $CO_2$-$H_2O$ contents to assess the effects of changing fluid composition ($XH_2O$) on Br fluid/melt partitioning for the first time. The experiments were conducted at pressures 50-120 MPa, temperatures 800°C – 1100°C and volatile compositions (molar $XH_2O = H_2O/(H_2O + CO_2)$) of 0.55 to 1, with redox conditions around the Nickel-Nickel Oxygen buffer ($fO_2 \approx$ NNO). Experiments were not doped with Cl, Br or F and were conducted on natural crystal-bearing volcanic products at conditions close to their respective pre-eruptive state. The experiments therefore provide realistic constraints on halogen partitioning at naturally occurring, brine-undersaturated conditions. Measurements of Br, Cl and F were made

by Secondary Ion Mass Spectrometry (SIMS) on thirteen experimental glass products spanning andesite to rhyolitic compositions, together with their natural starting materials from Kelud volcano, Indonesia, and Quizapu volcano, Chile. Fluid compositions were constrained by mass balance. Average bulk halogen fluid/melt partition coefficients and standard deviations are: $D_{Cl}^{fluid/melt}$ = 3.4 (± 3.7 1 s.d.) $D_{F}^{fluid/melt}$ = 1.7 (± 1.7) and $D_{Br}^{fluid/melt}$ = 7.1 (± 6.4) for the Kelud starting material (bulk basaltic andesite), and $D_{Cl}^{fluid/melt}$ = 11.1 (± 3.5), $D_{F}^{fluid/melt}$ = 0.8 (± 0.8) and $D_{Br}^{fluid/melt}$ = 31.3 (± 20.9) for Quizapu starting material (bulk dacite). The large range in average partition coefficients is a product of changing $XH_2O$, pressure and temperature. In agreement with studies on synthetic melts, our data show an exponential increase of halogen $D^{fluid/melt}$ with increasing ionic radius, with partitioning behaviour controlled by melt composition according to the nature of the complexes forming in the melt (e.g., $SiF_4$, NaCl, KBr). The fundamental chemistry of the different halogens (differing ionic size and electronegativities) controls the way in which partitioning responds to changes in melt composition, and other variables. Experimental results confirm that more Cl partitions into the fluid at higher bulk Cl contents, higher melt Na, higher fluid $XH_2O$ ratios and lower temperatures. Bromine shows similar behaviour, though seems to be more sensitive to temperature, and less sensitive to Na content and $XH_2O$. In contrast, F partitioning into the fluid increases as the melt silica content decreases (from 72 to 56 wt% $SiO_2$), which we attribute to the lower abundance of Si available to form F complexes in the melt. These new data provide more insights into the conditions and processes that control halogen degassing from magmas, and may help to inform the collection and interpretation of melt inclusions and volcano gas data.

## INTRODUCTION

Halogen behaviour in magmas impacts a range of crustal processes, including magma evolution, degassing and ore mineralisation, by influencing the physical and chemical properties of melts, fluids and minerals (Aiuppa et al. 2009; Pyle and Mather 2009; Bodnar et al. 2013; Harlov and Aranovich 2018; Webster et al. 2018). Although halogens may partition into crystals, gases and brine phases, this study concentrates on partitioning of halogens between the melt and aqueous fluid phase. Much previous work has concentrated on Cl, due to its ease of measurement in glasses by electron microprobe; and substantial advances in our understanding of Cl behaviour in melts can be attributed to J.D. Webster. Chlorine fluid/melt partitioning ($D_{Cl}^{fluid/melt}$) behaviour has been quantified for a range of silicate melt compositions (Webster and Holloway 1990; Webster 1997; Webster et al. 2014), pressures (Alletti et al. 2009; Botcharnikov et al. 2015; Webster et al. 2017), temperatures (Stelling et al. 2008), $fO_2$ (Beermann et al. 2015), and volatile contents (Lowenstern 1994; Botcharnikov et al. 2006; Alletti et al. 2009; Webster et al. 2014; Hsu et al. 2019). Fluorine, a relatively difficult element to measure in silicate glass (due to elemental interferences on the electron microprobe), has received less study, with most experiments focusing on end-member silicic or alkaline magmas (figure 1) (Webster and Holloway 1990; Borodulin et al. 2009; Iveson et al. 2017) and few data available for mafic and intermediate magmas (Chevychelov et al. 2008). Likewise, there are few data for bromine (figure 1) (Bureau et al. 2000; Bureau et al., 2010; Cadoux et al. 2018) because of its low abundance and analytical challenges. Nonetheless, the behaviour of bromine is of interest for its potential atmospheric impacts and detection of BrO in volcanic plumes by remote sensing (Aiuppa et al. 2005; Pyle and Mather 2009; Donovan et al. 2014; Gutmann et al. 2018).

The strong electronegativity of halogens largely controls their behaviour in magmas, and explains their propensity to form strong bonds, often with a high degree of polar or ionic

character. The differing electronegativities and ionic radii of the halogens lead to element-specific effects in melts and fluids (Dolejš and Zajacz 2018; Webster et al. 2018). For instance, the high electronegativity of F (relative to Cl and Br) promotes strong interactions with cations in silicate melts, enhancing its solubility in melts and thus lowering its degassing potential compared to the other halogens (Webster et al., 2018). During crystallisation of magmas the relatively small $F^-$ ion (1.33 Å) also substitutes effectively for similarly sized, $O^{2-}$ (1.26 Å) and $OH^-$ (1.32-1.37 Å) within the melt and is therefore thought to partition into silicate melts during volatile-undersaturated magma differentiation (e.g., Dolejš & Baker, 2007; Webster, 1990). In contrast, Cl and Br are thought to become less enriched in the melt during differentiation, as they partition to a fluid phase as melts become more silicic. Their larger ionic masses and radii, $Cl^-$ (1.81 Å) and $Br^-$ (1.95 Å) and the greater mismatch compared to $O^{2-}$ and $OH^-$ make Cl and Br less likely to be incorporated into the aluminosilicate network (Bureau et al., 2000) and promote a higher affinity with a coexisting aqueous fluid phase (Bureau et al. 2000; Bureau and Métrich 2003). Thus, Cl and Br fractionate more strongly into coexisting fluid during magmatic degassing compared with the lighter and smaller F (Teiber et al. 2014). Furthermore, the larger lattice energies for fluorides and higher hardness/bond strength as a ligand for complexing in comparison to chlorides, means a preference of F for the melt, and also the higher solubility of chlorides in aqueous fluids (Webster et al. 2015; Dolejš and Zajacz 2018).

The influence of melt composition on halogen behaviour is a product of the complexes they form with the cations in the melt. Chlorine dominantly dissolves in the melt by complexation with network modifying alkaline earth metals (Mg, Ca), alkalis (Na, K) and also Al and Fe, whereas it dissolves as an HCl species in aqueous magmatic fluids (Webster 1997; Webster and De Vivo 2002; Thomas and Wood 2020). Conversely, it is thought that F occurs in silicate melts as Si-F, Al-F, Na-F and Ca-F complexes (Dalou and Mysen 2015; Dalou et al. 2015; Bell and Simon 2011), while Br forms NaBr complexes at high pressure (>2 GPa) in hydrous felsic

melts (Cochain et al. 2015; Louvel et al. 2020). The effect of melt composition on F and Br fluid/melt partitioning is currently unclear, as few studies span intermediate to silicic melt compositions (Figure 1).

In magmatic systems the addition of volatiles such as $CO_2$ is known to influence the fluid/melt partitioning of chlorine: $D_{Cl}^{fluid/melt}$ decreases with increasing $CO_2$ addition, which is thought to be related to an increase of the activity coefficient for NaCl in the fluid phase, which decreases the stability of hydrated metal complexes in aqueous fluids, such as NaCl ion pairs (Alletti et al., 2009; Hsu et al., 2019). The effect of $CO_2$ on F and Br partitioning between fluid and melt is less studied, and our research assesses whether, like Cl, $CO_2$ presence in the fluid also decreases their fluid/melt partition coefficients. At low Cl concentrations <2.5 wt% in basaltic melts (Webster et al., 2015), and <0.25 wt% in rhyolitic melts (Zajacz et al. 2012), Cl fluid/melt partitioning exhibits Henrian behaviour where the increasing Cl content of the melt varies linearly with increasing Cl in the co-existing fluid. However, with increasing Cl concentrations, partitioning behaviour becomes non-linear and subsolvus fluid exsolution yields a lower density aqueous phase and a higher density hydrosaline brine (e.g., Webster et al. 1999; Shinohara 2009). We concentrate here on brine-undersaturated conditions, where halogen partitioning should follow Henrian behaviour and thus be more constant (Baker and Alletti, 2012). These conditions apply to the many active magmatic systems that have low halogen concentrations (Aiuppa et al. 2009) and lack a separate brine phase (Baker and Alletti 2012).

Recent experimental work by Thomas and Wood (2020) provides new insights into the chemical and thermodynamic basis for chlorine dissolution in silicate melts. The initial Cl dissolution into the melt involves the replacement of $O^{2-}$ by two dissociated $Cl^-$ ions:

$$Cl_2^{fluid} + [O^{2-}]^{melt} = 2[Cl^-]^{melt} + 0.5O_2^{fluid\ or\ melt}$$

This leads to a formulation for chlorine solubility in anhydrous basalts (Thomas & Wood 2020):

$$\mathrm{Log}(Cl^{melt}) = 0.984(64) - 930(70)P/T - 0.25\log(fO_2) + 0.5\log(fCl_2).$$

Where P is in GPa, T in K, and $fO_2$ and $fCl_2$ refer to the fugacities of a pure gas at 0.1 MPa and the temperature of interest. Values in brackets are 1 standard error of the last two digits for the corresponding experimentally determined constants.

This relationship predicts that in mafic systems at fixed $O_2$ and $Cl_2$ fugacities, increasing temperature should increase chlorine solubility of the melt (and therefore lower $D_{Cl}^{fluid/melt}$), while increasing pressure should decrease the chlorine solubility (and thus increase $D_{Cl}^{fluid/melt}$). While the relationship between $D^{fluid/melt}$ with temperature has been observed experimentally for Cl and Br, behaving in the same way (Webster et al., 2015; Cadoux et al., 2018), the results for F are less clear (Borodulin et al. 2009) and have been investigated in this study.

In this study we test the theoretical and experimental hypotheses described above, i.e., the role of ionic size, metal-ligand complexing, volatile composition ($H_2O$-$CO_2$) and variable temperature, on fluid/melt partitioning of F, Cl and Br. In particular we present new data on andesitic to rhyolitic melts to test whether i) classic phase equilibria experiments can be used for halogen partitioning determination, ii) the larger Cl and Br ions behave similarly to each other, preferring the fluid over the melt with the fluid preference increasing with increasing ionic radius, iii) F partitions into melt during differentiation whereas Cl and Br do not and instead associate with a fluid phase, iv) increasing temperature and $CO_2$ reduces partitioning of Cl into the fluid, along with other halogens.

## METHODS

### Experimental and analytical rationale

The experimental and analytical approach used in this study differs in several ways from previous studies. Our starting materials are deliberately tailored to specific magmatic systems, with the exact compositions, including the observed crystal assemblage, and the partition experiments run at pressures and temperatures which matched their pre-eruptive (experimentally-constrained) conditions (First et al. 2021; Cassidy et al. 2019). Capsules were not doped with added halogens. Only water ± carbon dioxide were added to reach fluid saturation. This approach was chosen to reproduce as close to 'real' conditions as the magmas experienced at their respective pre-eruptive storage conditions (e.g., 50-100 MPa for the bulk basaltic andesite composition of Kelud and 120 MPa for the bulk dacitic composition of Quizapu equating to 2-5 km depth) and to ensure pressure, temperature, and $X_{H2O}^{fluid}$, and brine-undersaturation conditions appropriate for the stored magmas (Cassidy et al. 2019; First et al. 2021). Due to the low concentrations and potential interferences, measurements were made by Secondary Ion Mass Spectrometry (SIMS). Despite the different experimental and analytical approach, we find encouragingly similar partitioning values compared to previously published experiments using synthetic and doped natural starting materials (Table S1).

This study focuses on two active and well-characterized systems, which are typical of subduction zone magmas undergoing crustal storage and degassing, and span the intermediate-silicic compositional range that is involved in the enrichment of metals and for which halogen partitioning data are least abundant (figure 1; Table S1; (Tattitch et al. 2021)). . Although some Cl data exist for compositions similar to Kelud and Quizapu (e.g., Zajacz et al., 2012), F and Br data are lacking, along with $H_2O$+CO2-bearing experiments at low pressures that allow us to understand their fluid/melt partitioning.

**Experimental procedure**

Natural samples of crystal-bearing basaltic-andesite from Kelud volcano and dacite from Quizapu volcano (IGSN: PPRAI101F) were used as starting materials. The Kelud basaltic andesite contains 50-60% crystals of plagioclase, ortho- and clinopyroxene, magnetite and matrix glass of dacite composition (Cassidy et al., 2016; Jeffery et al., 2013). The Quizapu dacite has a crystal content of 10-20 wt%, comprising plagioclase, amphibole, orthopyroxene, subordinate clinopyroxene, and accessory phases including apatite, titanomagnetite, ilmenite, sulfide blebs, and zircon, together with a mostly rhyolitic matrix glass (Ruprecht et al., 2012). These samples were coarsely crushed (sub mm size) to preserve the crystal cores. The cores act as nuclei, which become mantled by new crystal growth of a composition which is in equilibrium with the evolved matrix melt in the experiments. This ensures a realistic composition of the 'reactive melt' inside the shallow magmatic system (Pichavant et al. 2007; Erdmann et al. 2016). This approach was chosen as it more closely resembles natural conditions (i.e., melt, crystals and bubbles) and minimises concerns around structural changes to the melt and to the system overall, potentially affecting nucleation sites and crystallization kinetics, when starting from synthetic compounds or superliquidus conditions (Hammer 2008).

Approximately 0.1 g of sample was inserted into $Ag_{70}Pd_{30}$ capsules (wall thickness 0.25 mm), together with approximately 0.01 g distilled water using a micro syringe, which was enough to saturate the melt in $H_2O$ at the pressure and temperature of the experiments. The fluid to rock ratio was ~0.1 for most experiments; exact fluid masses were measured and used for subsequent mass balance calculations. For mixed volatile experiments $AgCO_3$ powder was added in specific molar proportions along with specific quantities of water (measured by mass), to generate water fractions ($X_{H2O}$) of 0.55 in the fluid phase (molar $X_{H2O} = H_2O/(H_2O + CO_2)$). $X_{H2O}$ of 0.55 was chosen to provide a contrasting but realistic value for comparison with pure water ($X_{H2O} = 1$) experiments. Capsules were sealed closed using an arc welder.

Experiments below 900 °C were conducted in hydrothermal cold seal pressure vessels (using Rene 41 autoclaves) at the University of Oxford, United Kingdom. For experiments exceeding 900 °C, gas-pressurized cold seals constructed ofh TZM (Tungsten-Zirconium-Molybdenum) alloy with argon as the pressurizing medium were used at the University of Mainz, Germany. To fix the oxygen fugacity for the gas pressured TZM experiments at the Nickel-Nickel-Oxygen buffer (NNO), a double-capsule technique was used, whereby Ni powder was added to a platinum foil capsule and left open to equilibrate with the melt (Shea & Hammer, 2013). In addition, methane was added as a reducing agent along with argon (0.4 MPa partial pressure), as tested in Shea and Hammer (2013). Ni metal powder (grey) oxidizes to green NiO, providing an easy visual check that the buffer is not exhausted at the end of the experiment. The oxidation conditions for the hydrothermal pressure vessels with Ni-Co alloy, Rene 41 autoclaves, were buffered at ~NNO by pure Nickel filler rods situated next to the capsule (Matthews et al., 2003).

A K-type thermocouple was inserted into a small hole in the end of the autoclave close to the capsule position to check for temperature offset between the furnace's internal thermocouple and autoclave. The samples were held at a constant pressure and temperature to replicate magmatic storage conditions for the specific volcanic systems, for up to 7 days (table 1), and the experiments were then rapidly quenched (<1 minute) in both cold seal and gas pressured experiments with a water-cooled system. Experimental run times were varied as a function of temperature, with a minimum of 25 hours for experiments at 1100 °C for basaltic andesite runs, and 160+ hours for silicic compositions and temperature of 800-900 °C. These run durations are similar to other partitioning studies with the shortest durations that reached equilibrium in 3-4 hours for chlorine partitioning experiments in basalts at 1200 °C (Alletti et al. 2009). However, Br diffusion is slower, which led Cadoux et al. (2018) to run their experiments at 1200 °C for 24 hours, the minimum time used in our experiments. For silicic compositions,

Kravchuk and Keppler (1994) ran partitioning experiments at 800 °C, varying run times between 93 and 1142 hours with little difference to measured halogen contents. Capsules were weighed before and after welding and following quenching of the experiments to ensure no fluid loss occurred; if mass loss was recorded, the experiments were discarded. Backscattered electron imaging of the run products showed microlite-free glass (figure S1) with little chemical variability (table 3).

## Analytical techniques

**Electron microprobe analysis (EMPA)**. The starting materials and experimental glasses were made into polished resin mounts (Epo thin 2) and carbon coated. They were analysed for their major element compositions by electron microprobe (EMPA) using a JEOL JXA 8200 superprobe at the University of Mainz and a Cameca SX-FiveFE at the University of Oxford. The operating conditions were: 15 kV accelerating voltage, 6-8 nA beam current, with a 10 µm defocussed beam and counting times of 50-200 s per analysis. Na and K peaks were counted first and for short (15 seconds) duration to minimise migration (Nielsen and Sigurdsson, 1981). Chlorine and fluorine were measured on the PETH and TAP crystals respectively, at counting times of 40 seconds each. A Phi-rho-Z correction for atomic number, absorption, and fluorescence was applied to all analyses, and the calibration was performed using a range of natural and synthetic reference materials. One sigma standard deviations were generally less than 2% for most major elements analysed. Secondary reference materials were measured on both EMPA instruments to ensure consistency and to assess the accuracy and precision, which can be found in table S2.

**Scanning Electron Microscope (SEM) image analysis**. Quantitative textural analysis of the glass was conducted using backscattered electron imagery combined with published energy dispersive spectrometer (EDS) mapping, from Cassidy et al. (2019). Carbon-coated

243 samples were imaged at 15 kV, a working distance of ~10 mm and spot size of ~50 µm using
244 a FEI Quanta 650 SEM at the University of Oxford. To measure the glass content of the initial
245 starting powder and final experimental products >10 back scattered electron images of each
246 sample were taken and ~300 crystals were digitised using image processing software. The glass
247 fraction was then quantified with ImageJ and is presented in Table 2.

248

249 **Secondary ion mass spectrometry (SIMS) analysis**.

250 The polished resin mounts were gold-coated (~30 nm thickness) and analysed on a Cameca
251 IMS 1270 instrument at the NERC ion microprobe facility at the University of Edinburgh. The
252 samples were placed in a vacuum to outgas for >14 hours prior to analyses. Vacuum in the
253 main chamber during analysis was $<5x10^{-8}$ Torr.

254 Halogen analyses were performed in two different sessions, both using a 10 kV, Cs+ primary
255 ion beam of ~2 nA for Cl and F, and ~7 nA for Br, with the normal incidence electron flood
256 gun for charge neutralisation and the electron multiplier (EM0) as the secondary ion detector.
257 After pre-sputtering for 60 s, the magnet calibration was checked and the automated secondary
258 beam alignment adjusted using either $^{18}O$ or $^{30}Si^{16}O_3$ as the reference peak.

259 For F and Cl analysis $^{18}O$, $^{19}F$, $^{30}Si$ and $^{35}Cl$ were measured at a mass resolution of 3,200, an
260 energy window of 60 eV, an analysed region of ~7 × 10 $\mu$m and magnetic peak switching. Each
261 analysis consisted of 10 cycles, in which $^{28}Si$ and $^{18}O$ were counted for 2 s each and $^{19}F$ and
262 $^{35}Cl$ for 4 s each. The secondary ion beam intensity measured at masses $^{19}F$ and $^{35}Cl$ were
263 normalized to $^{18}O$. To calculate the sample composition, we used MPI-DING reference glasses
264 (StHs80, ML-3BG, T1G, ATHO-G, Jochum et al. 2006) and the USGS reference glass BCR-
265 2G. The fluorine concentration of the unknown sample was given by:

$$F\ concentration = \left(\frac{^{19}F\ (cps)}{^{18}O\ (cps)}\right) * Relative\ Ion\ Yiel$$

Where the cps refers to counts per second, Relative Ion Yield = (Ion Yield F/ Ion Yield O) averaged over multiple primary standards, and

Ion Yield F = $^{19}$F (cps)/known F concentration

Ion Yield O = $^{18}$O (cps)/known O concentration

Chlorine concentrations were given by similar equations for the $^{35}$Cl count rate (cps) normalized to the $^{18}$O count rate (cps).

The standard deviation of the primary standard calibration of the Relative Ion Yields for F and Cl were lower than 4%.

For Br analysis, a mass resolution of 21,000 was used with a 2000 µm Field Aperture giving an analysed region of ~7 × 10 µm. Each analysis consisted of 10 measurement cycles with $^{30}Si^{16}O_3$ being measured for 2 s each cycle and $^{79}$Br and $^{81}$Br measured for 5 s each cycle. For Br we used GSC-1G, GSE-1G, GSD-1G, BB1 and BB2 (figure S2) as our standard reference materials (Marks et al. 2017; Kendrick 2012). The halogen concentrations of the unknown glasses were then calculated as follows:

$$Br\ concentration = \frac{^{81}Br\ (cps) + \ ^{79}Br\ (cps)}{(\ \ ^{30}SiO\ \ ^{16}O_3\ (cps)/(Si\ conc\ (known))} * Relative\ Ion\ Yiel$$

Where the Relative Ion Yield is given by= (Ion Yield of Br/ Ion Yield Si) for an average of multiple primary standards (table S2; figure S3) mounted in each sample block, and

Ion Yield Br = [$^{79}$Br (cps) + $^{81}$Br (cps)]/known Br concentration (primary standard),

Ion Yield Si = $^{30}Si^{16}O_3$ (cps)/known Si concentration (primary standard).

The Si content of the experiments was sometimes higher than the standards for Br (table S2), however as Br ionises well, as shown by relatively stable signal intensities, matrix glass effects are considered here to be minimal. This is supported by the secondary standard comparison plot (figure S2) for the five secondary standards, each with a different major element composition, showing a good match between measured and accepted values. Typically, seven analyses were measured per sample. Mean concentrations and standard deviations are given in table 3, and show good reproducibility. Along with the unknown samples, MPI-DING secondary reference glasses were measured throughout the analysis session to check for reproducibility, accuracy and drift (table S2). Limits of detection (estimated based on the number of counts per time counted, see table S2) for Cl and F were calculated on reference glasses StHs80 for F and Cl, and scapolite BB1 and GSE-1G for Br, equating to 0.5 ppm, 1.3 ppm and 0.35 ppm for F, Cl and Br respectively.

We found that the halogen concentrations for the secondary reference materials varied slightly between different mounts, potentially affected by the sample height, suggesting that calibration should be conducted on the same mounts as the sample analysis if possible.

## RESULTS

### Petrological description of run products

The run products range in glass contents from 28-47 wt% for Kelud, and 82-94 wt% in the Quizapu experiments (table 1). No new phases relative to the starting materials appeared during the experiments, however in some of the lower-temperature experiments, more evolved rims can be observed in backscattered images, compared to some more primitive crystal cores (figure S1). This suggests that mineral rims grew in equilibrium with the melt as intended by experimental design, without reacting with the more primitive mineral cores (Pichavant et al.,

2007). The experimental glass was microlite poor (figure S1), and contained vapour bubbles, indicative of fluid-saturation, which was confirmed by puncturing and heating the capsule post-experiment and determining relative mass loss. Repeat analyses of major element and halogen concentrations (n=7-24) of experimental glass showed them to be homogenous (fig. 2) within analytical uncertainty (table S3), suggesting that the time chosen to reach chemical equilibrium was appropriate (table 1).

**Halogen concentrations in matrix glass**

Although Cl measured both by electron microprobe (EMPA) and SIMS (figure S4), correlated fairly well, the concentrations of Cl were close to or below the limit of detection for EMPA, as the instrument set-up was not optimised for Cl measurements. We therefore report SIMS results in this paper, with their precision values <12%, and accuracy (<20% for Br, and <2% for Cl & F values >100 ppm) supported by analysis of secondary reference glasses (table S2).

The mean values, measured by SIMS, for the Kelud matrix glass composition (dacite) were: F = 564 ppm (+/- 56; 1 standard deviation of reproducibility), Cl = 1476 ppm (+/- 14), and Br = 4.3 ppm (+/- 0.4). For the Quizapu matrix glass composition (rhyolite): F = 661 ppm (+/- 44), Cl = 2192 ppm (+/- 100), and Br = 6.1 ppm (+/- 0.75) (table 2). Note that two bromine measurements of 0.42 ppm (Quiz 3) and 0.54 ppm (Quiz 5) are close to the detection limit of bromine of 0.35 ppm. Minor quantities of hydrous minerals (<1 % of halogen-bearing apatite and <2% amphibole in the Quizapu experiments) may slightly alter the absolute halogen contents in bulk starting material experiments.

Experimental matrix glass compositions range from andesitic to rhyolitic for Kelud (table 1; figure 2), with the Quizapu experiments limited to rhyolitic glass compositions (table 3). The range of compositions exhibited in the experimental glasses can be attributed to varying

amounts of melting and crystallisation resulting from the varying experimental run temperatures, fluid contents and compositions ($X_{H2O}$). Thus, variable crystallinity may dilute or enrich the halogen content in the glass for different experiments (table 1). Figure 2shows $SiO_2$ versus Cl, F and Br glass concentrations for all experiments. For the Kelud starting composition (Table 2), the experimental products with more evolved compositions contain higher F, Cl and Br concentrations in the natural matrix glass. These positive correlations with $SiO_2$ for fluorine ($R^2$= 0.68), chlorine ($R^2$ = 0.73) and bromine ($R^2$= 0.55) exist despite changes in experimental pressure, temperature and volatile composition. For the Quizapu starting composition (Table 2), this trend of increasing halogen concentrations at higher $SiO_2$ concentrations is apparent, despite the more limited range in compositions in the experimental matrix glass, e.g., for fluorine $R^2$=0.54. For chlorine and bromine the correlation only exists for the water saturated experiments ($X_{H2O}$ = 1), with correlation coefficients $R^2$ of 0.76, and 0.96 for Cl, and Br respectively. The mixed volatile experiments from Quizapu (green open symbols, figure 2) mostly fall within the same range as the water saturated experiments.

**Halogen fluid composition**

To work out the fluid composition required for calculating the fluid/melt partitioning, we used a simple mass balance approach similar to Cadoux et al. (2018):

$$Mass\ (g)\ of\ halogen\ in\ fluid = Mass\ of\ halogen\ in\ starting\ glass - Mass\ of\ halogen\ in\ final\ glass$$

Whereby,

Mass of halogen in starting powder = Concentration of halogen in starting powder (ppm)*$10^{-6}$ x Mass of starting powder (g).

The measured masses were converted into mass of glass, by correcting for the crystal fraction in the starting material and the final glass as measured with SEM image analysis (table 1).

358 *Mass (g) of halogen in the final glass = Concentration of halogen in final glass (ppm)*10$^{-6}$ x*
359 *Corrected mass of final glass (g)*

360 The corrected mass of the final glass is calculated from the initial mass of glass combined with
361 the mass of volatiles added to the capsule that dissolved within the melt. This correction
362 involves the respective gain and/or loss of water and $CO_2$, which partitioned from the volatile
363 phase in favour of the melt phase during the course of the experiment. These volatile contents
364 were modelled using a MELTS $H_2O$ and $CO_2$ solubility model, requiring the pressure,
365 temperature, $X_{H2O}$ and melt composition (Gualda and Ghiorso 2015). The modelled volatile
366 contents are comparable to other models (e.g., Papale et al., 2006).

367 *Fluid concentration of halogen (ppm)= mass (g) of halogen in fluid/ corrected final fluid*
368 *mass (g) x 10$^{6}$*

369 The uncorrected fluid mass was the measured weight of added volatiles to the capsule. The
370 mass difference between the final and initial glass was subtracted to give the corrected fluid
371 mass. At equilibrium during high P-T experiments there is a subtle impact of partial dissolution
372 of the aluminosilicate melt into the coexisting volatile phase (Burnham 1967). At the relatively
373 low pressures of these experiments, Burnham (1967) showed that only a small amount of solute
374 dissolved into the co-existing fluid (<2 wt%). A 2% correction was made to the masses of the
375 initial powder and volatile phase for all experiments. The partition coefficient for each halogen
376 was calculated by dividing the halogen concentration of the fluid by that of the melt.

377 Uncertainties were propagated using the minimum and maximum halogen concentrations in
378 the initial and experimental glasses, adjusting for crystal content calculation errors (+/- 5 wt%),
379 weighing errors and calculated masses of $H_2O$ and $CO_2$ (table 3). The propagated errors are
380 plotted in figures 4-8. Previous studies have shown that these propagated errors often
381 overestimate the absolute error and thus can be considered maximum values (e.g., Alletti et al.,

2014; Cadoux et al., 2018). Finally, Quizapu and Kelud both contain trace amounts of apatite (<1 vol%) and Quizapu contains ~2 vol% hornblende (Hildreth and Drake 1992 Ruprecht et al., 2012; Jeffery et al., 2014; Cassidy et al., 2016; 2019; First et al. 2021). Hydrous minerals may incorporate halogens into the mineral structure, but the low abundance of hydrous minerals, coupled with knowledge of mineral/melt partitioning values (e.g., Doherty et al., 2014; Iveson et al., 2017; Marks et al., 2017) suggests that minor amounts of crystallisation or melting of apatite and/or hornblende during the experiment would have a minimal effect on our $D^{fluid/melt}$ values. Given typical F and Cl contents in hornblende for Quizapu and arc magmas, this constitutes <10 ppm of Cl, and <50 ppm of F being added to the melt if hornblende is completely dissolved.

**Fluid/melt halogen partitioning**

No additional halogen sources were added to the starting materials and given that measured melt Cl contents are an order of magnitude below the modeled maximum Cl solubilities (Figure 3) (Webster et al., 2015), none of these experiments reached hydrosaline brine saturation, despite the addition of $CO_2$ in some experiments, which can lower the threshold for brine-saturation (Joyce and Holloway, 1992). The run product glasses lie within the experimentally constrained '200 MPa melt + aqueous vapour field' for rhyolitic melts in equilibrium with a low-density volatile phase (Webster et al., 2015, figure 3).

For all experiments, the halogen fluid concentrations show broad positive correlations with bulk fluid/melt partition coefficients consistent with other studies, and largely independent of temperature, pressure and volatile contents (Figures 4 and 5). Fluid concentration uncertainties were slightly higher for F and Br mass balance calculations, and these graphs show more scatter

than for Cl, which is a function of the larger range measured in glass halogen contents for these experiments. The mixed volatile experiments ($X_{H2O}$ = 0.55) fall on the generally positive trend, as do the higher pressure (100 MPa) Kelud experiments. A clear outlier to the generally positive correlations is Quiz 3 (850° C, $X_{H2O}$ = 1, Table 3), which yields higher than expected fluid/melt partitioning values relative to its fluid concentration (e.g., Figure 4). This can be attributed to a higher actual fluid mass than calculated, which is corroborated by the prominent $H_2O$ resorption haloes around the bubbles in the SEM images for Quiz 3 (figure S1). Consequently, this point was removed from the following dataset presented.

**Partitioning and Ionic radius**

Bureau et al. (2000) suggested that $D^{fluid/melt}$ increases with ionic radius for halogens in albite melt, although Cadoux et al., (2018) suggested further complexity to this relationship depending on melt composition and volatile content and based on deductions from gas geochemistry. The new experiments presented here are consistent with $D^{fluid/melt}$ increasing with ionic radius (Figure 5), though with higher $D_F^{fluid/melt}$ values than Bureau et al., (2000). On average, $D^{fluid/melt}$ for F (smallest ionic radius, D = 1.4 ± 0.51 (mean absolute error)) is lower than Cl (D = 6.4 ± 0.9), which is in turn lower than Br (largest ionic radius; D = 16.5 ± 6.5). These values are within the range measured for halogens in other studies on similar melt compositions (table S1). The average data can be fitted using an exponential function with a $R^2$ of 0.95, but the best fitted data is the Quizapu dataset shown in green (figure 5; $R^2$= 0.99). The less evolved Kelud experiments have a lower average bulk $D^{fluid/melt}$ than the more evolved Quizapu experiments for chlorine and bromine, but yield higher values for fluorine. This

observation may not be significant given the range of partitioning values, however it is consistent with the more evolved granitic melt value (76 wt% $SiO_2$ from Webster, (1990) for $D_F^{fluid/melt}$ which is even lower.

**Halogen fluid/melt partitioning as a function of changing intrinsic variables**

To assess the effects of varying melt composition on halogen $D^{fluid/melt}$, we plot our experimental data against the Larsen differentiation index $(0.33\times SiO_2+K_2O)-(FeO+MgO+CaO)$ (Larsen, 1938) (Figs. 6A, B & C). This has been shown to be a useful index for characterising evolving melt composition especially for Cl (e.g., Webster et al., 2020). It accounts for elements known to control Cl solubility (e.g. Ca, Mg and Fe; Webster et al., 2015), without using Na, which is prone to electron-beam migration in hydrous glasses. The Quizapu data show a very limited compositional change, yet a range in $D^{fluid/melt}$ (Figs. 6A, B & C). In contrast, the Kelud experimental glasses exhibit a wide range in glass compositions (andesite to rhyolite) and form shallow negative trends with respect to $D^{fluid/melt}$ with $R^2$ all above 0.72, with Cl particularly well correlated. In the case of fluorine, this trend extends towards the more evolved Quizapu compositions ($R^2$=0.5) (figure 6A). However, there is no significant trend with differentiation for Br and Cl when Kelud and Quizapu datasets are combined. The melt differentiation trends in the Kelud dataset occur despite superimposed differences in pressures, $CO_2$-$H_2O$ mixtures, temperatures and potential errors relating to the fluid calculation.

Kelud and Quizapu experiments show opposite trends as a function of temperature (figure 6D, E & F). While $D^{fluid/melt}$ in the Quizapu dacite series decreases with higher temperature, $D^{fluid/melt}$ in Kelud increases with temperature. The temperature effect on $D^{fluid/melt}$ values is most pronounced for the Quizapu dataset and for Br ($R^2$= 0.61), with F less temperature-dependent. Due to the large uncertainties of some Quizapu experiments, variance-weighted regression was

449 applied to temperature correlation, providing higher revised $R^2$ correlations of 0.82, 0.87, and
450 0.81, for F, Cl and Br respectively.

451 All experiments were fluid saturated, but mixed volatile experiments with varying $CO_2$ and
452 $H_2O$ ratios were run to assess their effect on fluid/melt partitioning of halogens (figure 6). In
453 both the Kelud and Quizapu dataset, the $CO_2$ bearing experiments ($X_{H2O}$ = 0.55) lie along the
454 same trends as the $X_{H2O}$ = 1 series, however the $CO_2$ bearing experiments generally show lower
455 $D^{fluid/melt}$ values (Figure 6). For the Kelud experiments, mean fluid/melt partition coefficients
456 for the $X_{H2O}$ = 1 experiments are F= 2 ± 1.9 (1 s.d), Cl = 4.4 ± 3.8, and Br = 8.8 ± 6.6 (n=6).
457 For the $X_{H2O}$ = 0.55 experiments these are F= 0.8 ± 0.3, Cl= 0.4 ± 0.4 and Br= 2.3 ± 0.1 (n=2).
458 For Quizapu, the $X_{H2O}$ = 1 experiments had mean fluid/melt ratios of; F= 0.1 ± 0.1, Cl= 9.3 ±
459 3.4, and Br= 22.7 ± 13.7 (n=2); whilst the $X_{H2O}$ = 0.55 experiments had $D^{fluid/melt}$ values; F= 1.4
460 ± 1.3, Cl= 12.3 ± 2.9 and Br= 37.1 ± 22.8, showing higher $D^{fluid/melt}$ values.

461 Figure 7 highlights in detail how $D^{fluid/melt}$ covaries with various elements for the combined
462 Kelud and Quizapu experimental dataset. Pearson correlation values suggest that $D_{Cl}^{fluid/melt}$
463 and $D_{Br}^{fluid/melt}$ generally behave in a similar way (correlation coefficient = 0.88), with highest
464 negative correlations for Ti (also Na in the case for Cl) and positive correlations Al and K.
465 While $D_F^{fluid/melt}$ behaves markedly differently from $D_{Cl}^{fluid/melt}$ and $D_{Br}^{fluid/melt}$ (coefficient = 0.24
466 and 0.26) and negatively correlates best with Si, Na, K, with positive correlations for Fe, Mg
467 and Ca. The differences between the Kelud and Quizapu datasets can be seen in figures S5 &
468 S6.

469 **Halogen fluid/melt partitioning across different studies**

470 Values for $D_{Cl}^{fluid/melt}$ are all <20 (figure 6B and E), in line with other studies at similar melt
471 compositions and experimental conditions (e.g., Baker & Alletti, 2012; Webster et al., 1999;
472 Zajacz et al., 2012) (table S1). The majority of experiments show that Cl predominantly

partitions into the fluid phase over the melt phase, with the exception of two Kelud experiments ($D_{Cl}^{fluid/melt}$ <1). Relative to Cl, absolute $D_F^{fluid/melt}$ values are lower (<6) with a cluster around 1 for the most differentiated melts. Values for Br partitioning are the highest among the halogens measured in this study, a trend observed by Bureau et al. (2000), with most partition coefficients ranging between 2 and 36 (table S1). In contrast to Cl and F, which partition into the melt under some conditions, our Br data show that it strongly partitions into the fluid phase in all the experiments.

Figure 8 plots our experiments in the context of other data from the literature (see figure S7 for full breakdown of the different studies). We use the aluminosity index A/CNK (molar Al/(Ca + Na + K), as Cl and F melt solubility are affected by increasing network-modifying Na, K and Ca relative to Al (figure 7) (Webster 1992; Signorelli and Carroll, 2000; Webster et al., 2015). The literature data plotted are from experiments thought to be in the brine-undersaturated region for Cl, F, and therefore thought to represent Henrian partitioning. This was estimated using the region of parameter space defined in previous studies (e.g., Cl <0.25 wt%, and F <4 wt%; cf., Baker & Alletti, 2012; Dolejš & Zajacz, 2018; Shinohara, 2009; Webster et al., 2015; Zajacz et al., 2012). However, some $CO_2$ bearing experiments from the literature may be in the brine field, as the presence of $CO_2$ lowers the threshold for brine saturation (e.g., Joyce and Holloway 1993). Figure 8 broadly highlights that the fluid/melt partition coefficients found in this study overlap with literature experiments at similar values on the aluminosity index. The Quizapu dataset for instance, has similar values to those of Alletti et al. (2009) and Botcharnikov et al. (2015), yet higher than others (Zajacz et al., 2012). Kelud's experimental glass composition also overlapped with other studies (Hsu et al., 2019; Webster et al., 2017; Webster & Holloway, 1990) and provides similar partitioning values. The literature data for $CO_2$ mixed volatile experiments on figure 8 are plotted as open circles and these generally occupy lower fluid/melt ratios for Cl (mean= 9.2, compared to water saturated experiments

(mean = 15), however their relative standard deviations both exceed 100%. For $CO_2$-bearing F partitioning experiments, there is only this study and a few data points from Webster et al. (2014) to compare (figure 8b), nevertheless the presence of $CO_2$ did not significantly influence $D_F^{fluid/melt}$. The only Br mixed volatile data are from this study and do not show significant differences with water-saturated experiments. Apart from the mixed volatile experiments, the data compilation in Figure 8 broadly shows that lower A/NCK values are associated with lower Br fluid/melt ratios (see also table S1). For F however, the opposite is true, with higher $D_F^{fluid/melt}$ values at the lower A/CNK values. There is no clear trend for $D_{Cl}^{fluid/melt}$, which speaks to the range of experimental conditions and the complexity of these data as well as the clustering of experiments in certain areas of A/CNK space (e.g., a sparsity of experiments at higher values).

# DISCUSSION

## Halogen Partitioning and its influences

The concentration of Cl in the fluid phase has been established as one of the primary controls on fluid melt partitioning (e.g., Webster, 1992), which is confirmed by this study for Cl and also for F and Br (figure 4). The scatter in the data, i.e., for a constant halogen fluid concentration, may be explained by the differing melt compositions and conditions (Dolejs & Zajacz, 2018). The sections below will cover how our experimentally derived halogen partitioning data are influenced by key variables such as ionic radius, melt composition, $X_{H2O}$ and temperature, in the context of previous studies. Whilst much of this has been studied for Cl, there is complexity (e.g. Figure 8), and fewer data points exist for F and Br (figure 1).

## Effect of ionic radius

Bureau et al. (2000) observed that for an albite melt composition, increasing fluid/melt partitioning values from F, Cl, Br to I correlate with increasing ionic radii of the anion (figure

522 5). This relationship has also been shown for the fluid/melt partitioning behaviour of the alkali
523 metals Li, K, and Rb (e.g., Iveson et al., 2019). This result agrees with previous studies which
524 dictate that for the larger anions (Cl and Br) there is a greater mismatch with the ionic radius
525 of O, making them less likely to be incorporated in the aluminosilicate network (Bureau et al.,
526 2000). The iodine partitioning data of Bureau et al. (2000) (Figure 5), can be used to extend
527 the partitioning – ionic radius correlation from our Quizapu (rhyolite glass) experiments
528 ($R^2$=0.99), which is more similar in composition to Bureau et al. (2000) than the Kelud dataset.
529 We use this correlation to form a revised weighted regression equation for rhyolitic melts based
530 on our experiments as a function of ionic radius:

531 $D_{Halogen}^{fluid/melt} = e^{(5.46(\pm0.09) \times Å - 7.41(\pm0.12))}$, where Å is the ionic radius in Angstrom.

532 The gradient of the slope (and thus the preceding equation), will vary as a result of the chemical
533 composition, for instance mafic melts with higher $D_F^{fluid/melt}$ (Fig 6 & 8) will lead to shallower
534 gradients and vice versa (e.g., Bureau et al., 2000). The large variability in these values means
535 that the highest $D_F^{fluid/melt}$ values are sometimes higher than the lowest $D_{Br}^{fluid/melt}$ values (Fig.
536 5), suggesting that other factors such as differences in halogen fluid concentrations, melt
537 compositions, pressure, temperature and $X_{H2O}$ may account for the variability in this trend.

538 **Effect of melt composition**

539 The two different starting compositions used in this study (whole rock basaltic andesite and
540 dacite, with dacitic and rhyolitic initial matrix glass compositions respectively) and variable P-
541 T conditions produced a range of different melt compositions, which allows us to explore the
542 role of composition on fluid/melt partitioning. Taking both datasets together, the highest
543 $D_{Cl}^{fluid/melt}$ and $D_{Br}^{fluid/melt}$ values are found in the most differentiated melts (Figure 6), yet the
544 least differentiated melts did not necessarily show the lowest fluid/melt partitioning. In

545 contrast, $D_F^{fluid/melt}$ shows the opposite trend across both datasets, with increasing
546 differentiation leading to lower average $D_F^{fluid/melt}$ values (Figure 6).

547 The notion of increased Cl in the fluid phase at more evolved compositions has been observed
548 in multiple studies (e.g., Webster and De Vivo, 2002) and also for Br (Cadoux et al., 2018).
549 This is likely related to the incompatible nature of the larger ions, Cl and Br in melts during
550 differentiation, lower charge densities of Cl and Br relative to F, coupled by the higher degree
551 of polymerisation, which makes the incorporation of larger anions into the melt more difficult.
552 More differentiated magmas have been predicted to have lower $D_F^{fluid/melt}$, based on the ability
553 of F to replace hydroxyl and oxygen ions in minerals, and substitute for O on the vertices of
554 aluminate or silicate tetrahedral, meaning that it preferentially favours the melt relative to fluid
555 phase as magma becomes more silicic during differentiation (Dolejš & Baker, 2007; Webster,
556 1990). Our data help to confirm this inference (figure 7) by filling a compositional gap in pre-
557 existing experimental data, and demonstrating higher $D_F^{fluid/melt}$, i.e., more F partitioning into
558 the fluid phase, in less evolved magmas.

559 Contrary to the overall observation of high $D_{Cl}^{fluid/melt}$ and $D_{Br}^{fluid/melt}$ for the most differentiated
560 magmas, within the Kelud dataset we find negative correlations with respect to $D_{Cl}^{fluid/melt}$, and
561 $D_{Br}^{fluid/melt}$ with differentiation (Figure 6), which exist despite removing the concentration of
562 halogens in the fluid as a factor. However, combining the Kelud and Quizapu datasets shows
563 no significant effect of differentiation (Figure 6), thus differentiation alone may not be able to
564 explain the distribution of $D_{Cl}^{fluid/melt}$ and $D_{Br}^{fluid/melt}$ values. The compositional influence on
565 partitioning may be more complex than mafic versus felsic, but instead related to the
566 availability of metal cations which form ligand complexes with F, Cl and Br. For instance, the
567 negative correlation between differentiation with $D_{Cl}^{fluid/melt}$ and $D_{Br}^{fluid/melt}$ for the Kelud
568 dataset, which encompasses a larger range of compositions than Quizapu (Figure 6), is likely
569 controlled by Na, K and Si complexes forming within these experimental melts (figure S5, S6).

Figure 7 combines both Quizapu and Kelud datasets and highlights the potential halogen complexes forming in all the experimental melts, by elements anti-correlated with $D^{fluid/melt}$ (e.g., K, Na, and Si for fluorine, Na, Ti for chlorine and Ti bromine). The type of metal-ligand bonds that form (e.g. Na-Cl, K-Cl) can be related to both the similarity in their orbital energy and the Lewis acidity or basicity of the cation and anion pair.

The latter can be conceptualised following the bond valence model from Brown (2000), which uses ion charge and coordination number to provide bond strength indicators in valence units (v.u.) for individual ions, which correlates with electronegativity. For instance, cations and anions with similar bond strengths (e.g., $Na^+$ – 0.16 v.u., and $Cl^-$ - 0.13 v.u.) and with the same number of atomic orbitals will be more likely to form strong associations, relative to cations that have larger bond strength differences, e.g., $Cl^-$ with $Ca^{2+}$ (0.27 v.u.) and less orbital overlap (e.g., K-Cl). These relationships are highlighted in the correlative plot in Figure 7, showing the $Na^+$ is anticorrelated with $D_{Cl}^{fluid/melt}$, whereas $Ca^{2+}$ and $K^+$ are not. It is possible that some of the positive elemental correlations with $D^{fluid/melt}$ in Figure 7 may indicate preferential complexes forming within the aqueous fluid (e.g., KCl, $CaF_2$, KBr). The negative correlations between Ti and $D_{Cl}^{fluid/melt}$ and $D_{Br}^{fluid/melt}$ (figure 7) are not found in either Kelud or Quizapu datasets separately, unlike other elemental correlations (Figures S5 & S6) and are therefore likely an artefact of bringing the two datasets together with inherently different Ti contents (Figure 7). The strong association between Si and F in our experiments (figure 7) is explained by high silicon-fluorine bond strength, resulting from their high charge densities (e.g., Dolejs and Baker, 2006; Dalou and Mysen, 2015). Some studies suggest that halide complexes with Mg, Ca, and Al are also important (Webster et al., 2015), but this was not observed in our study. The strong elemental associations in the melt observed here (e.g., NaCl, $SiF_4$) are more consistent with in situ spectroscopic measurements (Dalou et al., 2015; Louvel et al. 2020).

The inclusion of other volatile species such as sulfur, may also affect $D_{Cl}^{fluid/melt}$ by altering the nature of the complexes that form (Webster et al. 2009; Beermann, 2010). This effect seems to be dependent on the oxidation state, with $D_{Cl}^{fluid/melt}$ increasing with the addition of oxidised sulfur to the melts (Botcharnikov et al. 2004; Webster et al. 2003; Beermann 2010), due to the enhanced stabilisation of Na, K and Ca in S-bearing saline fluids. However, this effect is minimal at lower oxygen fugacities of NNO-0.5 (Zajacz et al. 2012). Sulfur concentrations were not measured here, but are likely be higher in the Quizapu samples, which evidenced by the presence of sulfide blebs visible under SEM (Ruprecht et al., 2012), compared to the Kelud samples where they were absent, and this may explain the different halide complexes formed in the melt (Na, K and Si for Kelud figure S5 & compared to Fe for Quizapu, figure S6). The reader is referred to Webster et al. (2020) for further discussion of the effect of oxidised vs. non-oxidised S on Cl solubility behaviour.

The alumina-saturation index (molar $Al_2O_3/(Na_2O+K_2O+CaO)$) has been shown to influence halogen fluid/melt and crystal/melt partitioning behaviour (e.g., Olin and Wolff 2012; Iveson et al. 2019), potentially accounting for some of the influence from these metal-ligand complexes (Fig. 8). Some broad trends of higher $D_{Br}^{fluid/melt}$ and lower $D_{F}^{fluid/melt}$ with increasing aluminosity exist, which can be attributed to presence or absence of Na, K complexes. However, there is significant scatter, partly due to the combination of different P-T experimental conditions, and partly because more elements than just Al, Na, K and Ca are involved in the formation of melt halide complexes.

**Effect of temperature**

There are relatively few experiments that attempt to assess the influence of temperature on halogen partitioning. Most data suggest that temperature has a minor effect on Cl, relative to the much stronger controls of melt and fluid composition (Chevychelov et al., 2008; Stelling

et al., 2008; Iveson et al., 2019). Bromine, however, may show stronger temperature dependence (Cadoux et al., 2018). Correlations between Cl, F and Br fluid/melt partitioning and temperature are clearly evident in our experiments (Figure 6), however for the Quizapu dataset this correlation is negative, with decreasing $D^{fluid/melt}$ values with increasing temperature, while the Kelud dataset shows the opposite trend. Because the temperature (and pressure) of the experiment can also affect its melt composition through the crystallisation or melting of mineral phases, it can be difficult to disentangle these two factors, especially since melt composition has a dominant role in controlling fluid/melt partitioning. Certainly for the Kelud experiments the change in the melt composition is large (58% - 73 wt% $SiO_2$; Figure 2), suggesting that the fluid/melt partitioning is most likely dominated by the change in melt composition, overprinting any temperature effect (Figure 6). However, for the Quizapu experiments there is a relatively smaller compositional change in the melt chemistry (69 - 74 wt% $SiO_2$; Figure 6). Therefore, the variation in experimental temperature (800 °C - 900 °C) likely explains the negative correlation of $D^{fluid/melt}$ observed for the Quizapu experiments. This concurs with the thermodynamic formulation from Thomas and Wood (2020) for anhydrous basalts, which also shows that Cl solubility in melt should increase with increasing temperature. This effect has been observed previously in experiments on Br partitioning, which show increasing $D_{Br}^{fluid/melt}$ with decreasing temperatures (900-1200 °C (Cadoux et al., 2018). The larger effect of temperature on $D_{Br}^{fluid/melt}$ compared to Cl (and especially F) may be related to the relatively weaker metal-ligand bonds formed by Br in the melt, due to its lower electronegativity and charge density, relative to Cl and F. The smaller ionic size of F leads to larger lattice energies of fluorides and therefore higher temperature stability of F complexes, which may explain the smaller temperature effect on $D_F^{fluid/melt}$.

**Effect of $CO_2$**

Five $H_2O$+$CO_2$-bearing experiments ($X_{H2O}$ = 0.55) were conducted in this study and are compared with fluid/melt partitioning values for the same composition, pressure and temperature conditions. The $X_{H2O}$ = 0.55 experiments follow similar compositional trends to those defined for $X_{H2O}$ = 1, suggesting that $CO_2$ did not have a strong influence on this trend (Figure 6). In the Kelud dataset the $X_{H2O}$ = 0.55 experiments show generally lower $D_{Cl}^{fluid/melt}$, however these were also more differentiated and so the effect of melt composition may also be a factor here (Fig. 6). Other studies suggest that the effect of $CO_2$ on $D_{Cl}^{fluid/melt}$ partitioning is variable, studies of andesitic, phonolitic and trachytic melts show that $CO_2$ in the fluid has little influence on $D_{Cl}^{fluid/melt}$ (Botcharnikov et al. 2006; Webster et al. 2014), whilst Alletti et al. (2009) observed decreasing values of $D_{Cl}^{fluid/melt}$ with increasing $CO_2$ in fluids coexisting with trachybasaltic melt at 25–100 MPa. Hsu et al. (2019) assessed the role of $CO_2$ systematically and found that $CO_2$ lowers $D_{Cl}^{fluid/melt}$. Following the empirical regression of Hsu et al. (2019) based on granitic melts, we found that this equation could not replicate the Cl partitioning values from our $CO_2$-$H_2O$ experiments, although this seems to be calibrated for slightly higher pressures than the run conditions of our experiments. Our compilation (Figure 8) suggests that average $D_{Cl}^{fluid/melt}$ ‘s for $H_2O$+$CO_2$ bearing experiments are lower than the pure $H_2O$ experiments, but this is not outside the variation of their ranges. There is a limited dataset of $CO_2$-bearing experiments to assess F and Br fluid/melt partitioning (Figure 8); these data suggest that $CO_2$ addition has only a minor effect on $D_F^{fluid/melt}$ and $D_{Br}^{fluid/melt}$ when compared with other effects such as fluid and melt composition, but this effect may differ for higher fluid salinity than used in this study.

## IMPLICATIONS

This study provides key information about halogen behaviour in intermediate to silicic melts, compositions typical of those produced in subduction zone magmas, which have received far less study to date (Figure 1), but commonly result in hazardous explosive eruptions and the

667 generation of ores. Data across a wide range of compositions are required to build rigorous
668 models of halogen behaviour during volcanic processes. Using the approach outlined here of
669 not doping experiments with halogens, but analysing low concentrations with SIMS, opens up
670 the potential for the measurement of halogens in previously conducted phase equilibria
671 experiments. Our analysis supports the notion that melt composition has a strong control on Cl,
672 F and Br fluid/melt partitioning (e.g. Webster et al., 2018). Simple differentiation does not
673 control the variation of partitioning values for Cl and Br partitioning (Figure 6). Instead,
674 particular elements (e.g., K, Al, Na) with an affinity to make complexes with Cl and Br in the
675 melt, can explain 40 to 60 % of the variation in Br and Cl fluid/melt partition coefficients
676 (Figure 7). In contrast, F seems to favour the melt over the fluid with increasing differentiation,
677 with >70% of the variation in $D_F^{fluid/melt}$ explained by Si concentration alone (Figure 2, Figure
678 7). This observation may be applied to the interpretation of magmatic processes in melt
679 inclusions and hydrous minerals (retrospectively), or volcanic gas monitoring (in real time).
680 For instance, measurements of volcanic gas species are used to interpret changing depth of
681 magma, since $H_2O$, S and $CO_2$ solubilities are particularly sensitive to pressure and oxidation
682 state (e.g., de Moor et al., 2016). However if S, $H_2O$ and $CO_2$ fluxes, and associated ratios
683 remain constant, but halogen ratios such as (Cl+Br)/F ratios increase over time, this could point
684 to differentiation, or even temperature changes of an underlying stationary magma reservoir
685 (e.g., Aiuppa et al. 2002, 2007; Edmonds et al. 2003, 2009; Allard et al. 2005; Burton et al.
686 2007; Balcone-Boissard et al. 2010; Bobrowski and Giuffrida 2012; Christopher et al. 2015).
687 The strong relationship of $D_F^{fluid/melt}$ with melt composition, which decreases both with
688 differentiation (Figure 6) and degree of aluminosity (Figure 8), might also explain the higher
689 extent of F degassing in basaltic and alkaline lava lakes relative to silicic stratovolcanoes; the
690 former may be accentuated by gas exsolution in equilibrium at shallow pressures, <10 MPa
691 (e.g., Edmonds et al. 2009; Oppenheimer et al. 2011). Individual magmatic volatile species are

692 variably affected by different magmatic processes and conditions, such that by measuring a
693 larger set of volatile species in melt inclusions, such as $CO_2$, $H_2O$, S along with F, Cl, and Br,
694 one may be able to disentangle these magmatic conditions and processes prior to eruptions. For
695 instance, trends towards higher (Cl+Br)/F melt ratios may indicate mafic injection due to the
696 compositional effects, whereas trends to lower (Cl+Br)/F ratios, with increasing $H_2O$, and
697 relatively constant S, may point to differentiation of a stationary magma reservoir leading to
698 second boiling. By providing more fluid/melt partitioning data for a range of subduction zone
699 magma compositions, these will also aid the calculation (e.g., via the melt inclusion
700 petrological method) of Cl, F and Br fluxes into the atmosphere for historical eruptions sourced
701 from intermediate and silicic magmas, which have the potential for significant stratospheric
702 ozone destruction (e.g. Kutterolf et al. 2013; Cadoux et al. 2015; Vidal et al., 2016; Cadoux et
703 al., 2015).

704

705 **Acknowledgements**

706 M.C. acknowledges funding from NERC Independent Research fellowship NE/N014286/1.
707 A.A.I. is currently funded by the Leverhulme Trust through an Early Career Fellowship P.R.
708 acknowledges funding from US NSF grant EAR 1347880/1717288. Vitaly Chevchelov is
709 thanked for the inclusion of compositional data. We thank Jon Wade and Phil Gopon for
710 electron microprobe assistance, and Richard Thomas and Bernie Wood for discussion. Thor
711 Hansteen and an anonymous reviewer are thanked for their helpful comments to improve this
712 paper.

713 **Figure Captions:**

714 Figure 1. Total alkali silica plot for all the previous brine undersaturated experiments, along
715 with their corresponding pressures (MPa), for chlorine, fluorine and bromine. The grey

716 symbols represent the compositional space that the experiments in this study cover at
717 pressures of 50 to 120 MPa. References for the data found in Table S1.

718 Figure 2. SiO2 versus halogen concentrations in experimental glass products, along with their
719 natural matrix glass compositions. Errors given are 1 standard deviation of the range of the
720 values measured.

721 Figure 3. Showing Cl melt contents of the experiments of Quizapu, dacite starting material
722 (green) and Kelud, basaltic andesite starting material (blue), with the corresponding modelled
723 H2O contents from MELTS. The dashed lines indicate where brine and vapor phases appear
724 at 50 MPa and 200 MPa pressures. The crosses indicate the maximum Cl contents for each
725 experiment as modelled using Webster et al., 2015 Cl solubility model. Our experiments
726 show brine under-saturated conditions.

727 Figure 4. Mass balance calculated fluid halogen concentrations, against halogen fluid-melt
728 partitioning. Maximum accumulated errors are plotted.

729 Figure 5. Plot of natural log of fluid/melt F, Cl and Br partitioning values in this study and
730 iodine value from Bureau, 2000 against ionic radius in Angstroms. For comparison the
731 dataset and trendline from Bureau et al., (2000) is plotted.The green trendline shown is from
732 the Quizapu dataset, which represents the best correlation. Error bars indicate 1 standard
733 deviation of the values for the pressures (50-120 MPa), temperatures (800°C – 1100°C ) and
734 XH2O (0.55-1) conditions. The biggest difference is the differing F partitioning values
735 (higher in this study) which alters the regression equation. The F partitioning value in Bureau
736 et al., (2000), was from Webster et al., (1992), measured in granitic melts.

737 Figure 6. Effects of glass composition (Larsen differentiation) and temperature on bulk
738 partitioning of halogens. R2 values shown above report both the unweighted and weighted
739 regressions. Variance-weighted regression was applied to Quizapu dataset which has higher

740 uncertainties (D, E and F), providing revised R2 values and the trend lines against
741 temperature plotted above.

742 Figure 7. Scatter plot of matrices of different elements and the Cl, F and Br partitioning
743 values, with bivariate scatter plots below the diagonal, histograms on the diagonal, and the
744 Pearson correlation above the diagonal. The key correlations are highlighted in red. In the
745 scatter plots the X axes represent the range of values of the element in the same row, while
746 the Y axes represent the element in the vertical column.

747 Figure 8. The molar Aluminium/Calcium+Sodium+Potassium ratio for data in these study as
748 a comparison to data from literature (including CO2 bearing systems) for non-brine systems,
749 and therefore thought to represent henrian partitioning. Literature sources in table S1 and
750 broken down by study in figure S7.

751 **REFERENCES**

752 Aiuppa, A., Federico, C., Paonita, A., Pecoraino, G., and Valenza, M. (2002) S, Cl and F
753 degassing as an indicator of volcanic dynamics: The 2001 eruption of Mount Etna.
754 Geophysical Research Letters, 29, 1–4.

755 Aiuppa, A., Federico, C., Franco, A., Giudice, G., Gurrieri, S., Inguaggiato, S., Liuzzo, M.,
756 McGonigle, A.J.S., and Valenza, M. (2005) Emission of bromine and iodine from
757 Mount Etna volcano. Geochemistry, Geophysics, Geosystems, 6, 1–8.

758 Aiuppa, A., Moretti, R., Federico, C., Giudice, G., Gurrieri, S., Liuzzo, M., Papale, P.,
759 Shinohara, H., and Valenza, M. (2007) Forecasting Etna eruptions by real-time
760 observation of volcanic gas composition. Geology, 35, 1115–1118.

761 Aiuppa, A., Baker, D.R., and Webster, J.D. (2009) Halogens in volcanic systems. Chemical
762 Geology, 263, 1–18.

763 Allard, P., Burton, M., and Mur, F. (2005) Spectroscopic evidence for a lava fountain driven
764 by previously accumulated magmatic gas. Nature, 433, 407–410.

765 Alletti, M., Baker, D.R., Scaillet, B., Aiuppa, A., Moretti, R., and Ottolini, L. (2009) Chlorine
766 partitioning between a basaltic melt and $H_2O$-$CO_2$ fluids at Mount Etna. Chemical
767 Geology, 263, 37–50.

768 Alletti, M., Burgisser, A., Scaillet, B., and Oppenheimer, C. (2014) Chloride partitioning and
769 solubility in hydrous phonolites from Erebus volcano: A contribution towards a multi-
770 component degassing model. GeoResJ, 3–4, 27–45.

771 Baker, D.R., and Alletti, M. (2012) Fluid saturation and volatile partitioning between melts
772 and hydrous fluids in crustal magmatic systems: The contribution of experimental
773 measurements and solubility models. Earth-Science Reviews, 114, 298–324.

774 Balcone-Boissard, H., Villemant, B., and Boudon, G. (2010) Behavior of halogens during the
775 degassing of felsic magmas. Geochemistry, Geophysics, Geosystems, 11.

776 Beermann, O., Botcharnikov, R.E., and Nowak, M. (2015) Partitioning of sulfur and chlorine
777 between aqueous fluid and basaltic melt at 1050°C, 100 and 200 MPa. Chemical
778 Geology, 418, 132–157.

779 Bell, A.S., and Simon, A. (2011) Experimental evidence for the alteration of the $Fe^{3+}/\Sigma Fe$ of
780 silicate melt caused by the degassing of chlorine-bearing aqueous volatiles. Geology, 39,
781 499–502.

782 Bobrowski, N., and Giuffrida, G. (2012) Bromine monoxide/sulphur dioxide ratios in relation
783 to volcanological observations at Mt. Etna 2006-2009. Solid Earth, 3, 433–445.

784 Bodnar, R.J., Lecumberri-Sanchez, P., Moncada, D., and Steele-MacInnis, M. (2013) Fluid
785 Inclusions in Hydrothermal Ore Deposits. In Treatise on Geochemistry: Second Edition.

786 Borodulin, G.P., Chevychelov, V.Y., and Zaraysky, G.P. (2009) Experimental study of
787 partitioning of tantalum, niobium, manganese, and fluorine between aqueous fluoride
788 fluid and granitic and alkaline melts. Doklady Earth Sciences, 427, 868–873.

789 Botcharnikov, R.E., Behrens, H., and Holtz, F. (2006) Solubility and speciation of C-O-H
790 fluids in andesitic melt at T = 1100-1300 °C and P = 200 and 500 MPa. Chemical
791 Geology, 229, 125–143.

792 Botcharnikov, R.E., Holtz, F., and Behrens, H. (2015) Solubility and fluid-melt partitioning
793 of H2O and Cl in andesitic magmas as a function of pressure between 50 and 500 MPa.
794 Chemical Geology, 418, 117–131.

795 Brown, I.D. (2000) The Bond Valence Model as a Tool for Teaching Inorganic Chemistry:
796 The Ionic Model Revisited. Journal of Chemical Education, 77, 1070–1075.

797 Bureau, H., and Métrich, N. (2003) An experimental study of bromine behaviour in water-
798 saturated silicic melts. Geochimica et Cosmochimica Acta, 67, 1689–1697.

799 Bureau, H., Keppler, H., and Métrich, N. (2000) Volcanic degassing of bromine and iodine:
800 Experimental fluid/melt partitioning data and applications to stratospheric chemistry.
801 Earth and Planetary Science Letters, 183, 51–60.

802 Burnham (1967) Hydrothermal fluids at the magmatic stage. In Geochemistry of
803 Hydrothermal Ore Deposits pp. 34–76. Holt, Rinehart, and Winston, New York.

804 Burton, M., Allard, P., Mure, F., and La Spina, A. (2007) Magmatic gas composition reveals
805 the source depth of slug-driven strombolian explosive activity. Science.

806 Cadoux, A., Scaillet, B., Bekki, S., Oppenheimer, C., and Druitt, T.H. (2015) Stratospheric
807 Ozone destruction by the Bronze-Age Minoan eruption (Santorini Volcano, Greece).
808 Scientific Reports, 5, 1–12.

809 Cadoux, A., Iacono-Marziano, G., Scaillet, B., Aiuppa, A., Mather, T.A., Pyle, D.M.,
810 Deloule, E., Gennaro, E., and Paonita, A. (2018) The role of melt composition on
811 aqueous fluid vs. silicate melt partitioning of bromine in magmas. Earth and Planetary
812 Science Letters, 498, 450–463.

813 Cassidy, M., Castro, J.M., Helo, C., Troll, V.R., Deegan, F.M., Muir, D., Neave, D.A., and
814 Mueller, S.P. (2016) Volatile dilution during magma injections and implications for
815 volcano explosivity. Geology, 44, 1027–1030.

816 Cassidy, M., Ebmeier, S.K., Helo, C., Watt, S.F.L., Caudron, C., Odell, A., Spaans, K.,
817 Kristianto, P., Triastuty, H., Gunawan, H., and others (2019a) Explosive Eruptions With
818 Little Warning: Experimental Petrology and Volcano Monitoring Observations From the
819 2014 Eruption of Kelud, Indonesia. Geochemistry, Geophysics, Geosystems, 1–30.

820 Cassidy, M., Ebmeier, S.K., Helo, C., Watt, S.F.L., Caudron, C., Odell, A., Spaans, K.,
821 Kristianto, P., Triastuty, H., Gunawan, H., and others (2019b) Explosive Eruptions With
822 Little Warning: Experimental Petrology and Volcano Monitoring Observations From the
823 2014 Eruption of Kelud, Indonesia. Geochemistry, Geophysics, Geosystems, 20.

824 Chevychelov, V.Y. (2019) Partitioning of Volatile Components (Cl, F, and $CO_2$) in Water-
825 Saturated Fluid–Magma Systems of Various Composition. Petrology, 27, 585–605.

826 Chevychelov, V.Y., Bocharnikov, R.E., and Holtz, F. (2008) Experimental study of chlorine
827 and fluorine partitioning between fluid and subalkaline basaltic melt. Doklady Earth
828 Sciences, 422, 1089–1092.

829 Christopher, T.E., Blundy, J., Cashman, K., Cole, P., Edmonds, M., Smith, P.J., Sparks,
830 R.S.J., and Stinton, A. (2015) Crustal-scale degassing due to magma system
831 destabilization and magma-gas decoupling at Soufrière Hills Volcano, Montserrat.
832 Geochemistry, Geophysics, Geosystems, 16, 2797–2811.

833 Cochain, B., Sanloup, C., de Grouchy, C., Crépisson, C., Bureau, H., Leroy, C., Kantor, I.,
834 and Irifune, T. (2015) Bromine speciation in hydrous silicate melts at high pressure.
835 Chemical Geology.

836 Dalou, C., and Mysen, B.O. (2015) The effect of $H_2O$ on F and Cl solubility and solution
837 mechanisms of in aluminosilicate melts at high pressure and high temperature. American
838 Mineralogist.

839 Dalou, C., Mysen, B.O., and Foustoukos, D. (2015) In-situ measurements of fluorine and
840 chlorine speciation and partitioning between melts and aqueous fluids in the $Na_2O$-
841 $Al_2O_3$-$SiO_2$-$H_2O$ system. American Mineralogist, 100, 47–58.

842 Doherty, A.L., Webster, J.D., Goldoff, B.A., and Piccoli, P.M. (2014) Partitioning behavior
843 of chlorine and fluorine in felsic melt-fluid(s)-apatite systems at 50MPa and 850-950 °C.
844 Chemical Geology, 384, 94–109.

845 Dolejš, D., and Baker, D.R. (2007) Liquidus equilibria in the system $K_2O$-$Na_2O$-$Al_2O_3$-$SiO_2$-
846 $F_2O$-1-$H_2O$ to 100 MPa: II. Differentiation paths of fluorosilicic magmas in hydrous
847 systems. Journal of Petrology.

848 Dolejš, D., and Zajacz, Z. (2018) Halogens in Silicic Magmas and Their Hydrothermal
849 Systems. The Role of Halogens in Terrestrial and Extraterrestrial Geochemical
850 Processes: Surface, Crust, and Mantle

851 Donovan, A., Tsanev, V., Oppenheimer, C., and Edmonds, M. (2014) Reactive halogens
852 (BrO and OClO) detected in the plume of Soufrière Hills Volcano during an eruption
853 hiatus. Geochemistry, Geophysics, Geosystems.

854 Edmonds, M., Herd, R.A., Galle, B., and Oppenheimer, C.M. (2003) Automated, high time-
855 resolution measurements of $SO_2$ flux at Soufriere Hills Volcano, Montserrat. Bulletin of

856 Volcanology, 65, 578–586.

857 Edmonds, M., Gerlach, T.M., and Herd, R.A. (2009) Halogen degassing during ascent and
858 eruption of water-poor basaltic magma. Chemical Geology, 263, 122–130.

859 Erdmann, S., Martel, C., Pichavant, M., Bourdier, J.L., Champallier, R., Komorowski, J.C.,
860 and Cholik, N. (2016) Constraints from phase equilibrium experiments on pre-eruptive
861 storage conditions in mixed magma systems: A case study on crystal-rich basaltic
862 andesites from Mount Merapi, Indonesia. Journal of Petrology, 57, 535–560.

863 First, E.C., Hammer, J.E., Ruprecht, P., and Rutherford, M. (2021) Experimental constraints
864 on dacite magma storage beneath Volcán Quizapu, Chile. Journal of Petrology.

865 Gualda, G.A.R., and Ghiorso, M.S. (2015) MELTS-Excel: A Microsoft Excel-based MELTS
866 interface for research and teaching of magma properties and evolution. Geochemistry,
867 Geophysics, Geosystems, 16, 315–324.

868 Gutmann, A., Bobrowski, N., Roberts, T.J., Rüdiger, J., and Hoffmann, T. (2018) Advances
869 in bromine speciation in volcanic plumes. Frontiers in Earth Science, 6, 1–24.

870 Hammer, J.E. (2008) Experimental studies of the kinetics and energetics of magma
871 crystallization. Reviews in Mineralogy and Geochemistry.

872 Harlov, D.E., and Aranovich, L. (2018) The Role of Halogens in Terrestrial and
873 Extraterrestrial Geochemical Processes: Surface, Crust, and Mantle.

874 Hildreth, W., and Drake, R.E. (1992) Volcán Quizapu, Chilean Andes. Bulletin of
875 Volcanology, 54, 93–125.

876 Hsu, Y.J., Zajacz, Z., Ulmer, P., and Heinrich, C.A. (2019) Chlorine partitioning between
877 granitic melt and $H_2O$-$CO_2$-NaCl fluids in the Earth's upper crust and implications for
878 magmatic-hydrothermal ore genesis. Geochimica et Cosmochimica Acta, 261, 171–190.

879 Iveson, A.A., Webster, J.D., Rowe, M.C., and Neill, O.K. (2017) Major element and halogen
880 (F, Cl) mineral-melt-fluid partitioning in hydrous rhyodacitic melts at shallow crustal
881 conditions. Journal of Petrology, 58, 2465–2492.

882 ——— (2019) Fluid-melt trace-element partitioning behaviour between evolved melts and
883 aqueous fluids: Experimental constraints on the magmatic-hydrothermal transport of
884 metals. Chemical Geology, 516, 18–41.

885 Jeffery, A.J., Gertisser, R., Troll, V.R., Jolis, E.M., Dahren, B., Harris, C., Tindle, A.G.,
886 Preece, K., O'Driscoll, B., Humaida, H., and others (2013) The pre-eruptive magma
887 plumbing system of the 2007-2008 dome-forming eruption of Kelut volcano, East Java,
888 Indonesia. Contributions to Mineralogy and Petrology, 166, 275–308.

889 Jochum, K.P., Stoll, B., Herwig, K., Willbold, M., Hofmiann, A.W., Amini, M., Aarburg, S.,
890 Abouchami, W., Hellebrand, E., Mocek, B., and others (2006) MPI-DING reference
891 glasses for in situ microanalysis: New reference values for element concentrations and
892 isotope ratios. Geochemistry, Geophysics, Geosystems, 7.

893 Joyce, D.B., and Holloway, J.R. (1993) An experimental determination of the thermodynamic
894 properties of H2O-CO2-NaCl fluids at high pressures and temperatures. Geochimica et
895 Cosmochimica Acta, 57, 733–746.

896 Kendrick, M.A. (2012) High precision Cl, Br and I determinations in mineral standards using
897 the noble gas method. Chemical Geology, 292–293, 116–126.

898 Kutterolf, S., Hansteen, T.H., Appel, K., Freundt, A., Krüger, K., Pérez, W., and Wehrmann,
899 H. (2013) Combined bromine and chlorine release from large explosive volcanic
900 eruptions: A threat to stratospheric ozone? Geology, 41, 707–710.

901 Louvel, M., Cadoux, A., Brooker, R.A., Proux, O., and Hazemann, J.L. (2020) New insights

902 on Br speciation in volcanic glasses and structural controls on halogen degassing.
903 American Mineralogist, 105, 795–80

904 Lowenstern, J.B. (1994) Chlorine, fluid immiscibility, and degassing in peralkaline magmas
905 from Pantelleria, Italy. American Mineralogist, 79, 353–369.

906 Marks, M.A.W., Wenzel, T., Whitehouse, M.J., Loose, M., Zack, T., Barth, M., Worgard, L.,
907 Krasz, V., Eby, G.N., Stosnach, H., and others (2012) The volatile inventory (F, Cl, Br,
908 S, C) of magmatic apatite: An integrated analytical approach. Chemical Geology, 291,
909 241–255.

910 Marks, M.A.W., Kendrick, M.A., Eby, G.N., Zack, T., and Wenzel, T. (2017) The F, Cl, Br
911 and I Contents of Reference Glasses BHVO-2G, BIR-1G, BCR-2G, GSD-1G, GSE-1G,
912 NIST SRM 610 and NIST SRM 612. Geostandards and Geoanalytical Research, 41,
913 107–122.

914 Moor, J.M., Aiuppa, A., Avard, G., Wehrmann, H., Dunbar, N., Muller, C., Tamburello, G.,
915 Giudice, G., Liuzzo, M., Moretti, R., and others (2016) Turmoil at Turrialba Volcano
916 (Costa Rica): Degassing and eruptive processes inferred from high-frequency gas
917 monitoring. Journal of Geophysical Research: Solid Earth, 1–15.

918 Olin, P.H., and Wolff, J.A. (2012) Partitioning of rare earth and high field strength elements
919 between titanite and phonolitic liquid. Lithos.

920 Oppenheimer, C., Moretti, R., Kyle, P.R., Eschenbacher, A., Lowenstern, J.B., Hervig, R.L.,
921 and Dunbar, N.W. (2011) Mantle to surface degassing of alkalic magmas at Erebus
922 volcano, Antarctica. Earth and Planetary Science Letters.

923 Papale, P., Moretti, R., and Barbato, D. (2006) The compositional dependence of the
924 saturation surface of $H_2O$ + $CO_2$ fluids in silicate melts. Chemical Geology, 229, 78–95.

925 Pichavant, M., Costa, F., Burgisser, A., Scaillet, B., Martel, C., and Poussineau, S. (2007)
926 Equilibration scales in silicic to intermediate magmas - Implications for experimental
927 studies. Journal of Petrology, 48, 1955–1972.

928 Pyle, D.M., and Mather, T.A. (2009) Halogens in igneous processes and their fluxes to the
929 atmosphere and oceans from volcanic activity: A review. Chemical Geology, 263, 110–
930 121.

931 Ruprecht, P., and Bachmann, O. (2010) Pre-eruptive reheating during magma mixing at
932 Quizapu volcano and the implications for the explosiveness of silicic arc volcanoes.
933 Geology, 38, 919–922.

934 Ruprecht, P., Bergantz, G.W., Cooper, K.M., and Hildreth, W. (2012) The crustal magma
935 storage system of volcán Quizapu, Chile, and the effects of magma mixing on magma
936 diversity. Journal of Petrology, 53, 801–840.

937 Shinohara, H. (2009) A missing link between volcanic degassing and experimental studies on
938 chloride partitioning. Chemical Geology, 263, 51–59.

939 Sigurdsson, N.& (1981) NielsenQuantitative methods for electron microprobe analysis of
940 sodium in natural and synthetic glasses American Mineralogist2004.pdf.

941 Stelling, J., Botcharnikov, R.E., Beermann, O., and Nowak, M. (2008) Solubility of $H_2O$- and
942 chlorine-bearing fluids in basaltic melt of Mount Etna at T = 1050-1250 °C and P =
943 200 MPa. Chemical Geology, 256, 101–109.

944 Tattitch, B., Chelle-Michou, C., Blundy, J., and Loucks, R.R. (2021) Chemical feedbacks
945 during magma degassing control chlorine partitioning and metal extraction in volcanic
946 arcs. Nature Communications, 12.

947

948 Teiber, H., Marks, M.A.W., Wenzel, T., Siebel, W., Altherr, R., and Markl, G. (2014) The
949 distribution of halogens (F, Cl, Br) in granitoid rocks. Chemical Geology, 374–375, 92–
950 109.

951 Thomas, R.W., and Wood, B.J. (2020) The chemical behaviour of chlorine in silicate melts.
952 Geochimica et Cosmochimica Acta.

953 Vidal, C.M., Métrich, N., Komorowski, J.-C., Pratomo, I., Michel, A., Kartadinata, N.,
954 Robert, V., and Lavigne, F. (2016) The 1257 Samalas eruption (Lombok, Indonesia): the
955 single greatest stratospheric gas release of the Common Era. Scientific Reports, 6,
956 34868.

957 Webster, J.D. (1990) Partitioning of F between $H_2O$ and $CO_2$ fluids and topaz rhyolite melt -
958 Implications for mineralizing magmatic-hydrothermal fluids in F-rich granitic systems.
959 Contributions to Mineralogy and Petrology, 104, 424–438.

960 ——— (1992) Water solubility and chlorine partitioning in Cl-rich granitic systems: Effects
961 of melt composition at 2 kbar and 800°C. Geochimica et Cosmochimica Acta.

962 ——— (1997) Exsolution of magmatic volatile phases from Cl-enriched mineralizing
963 granitic magmas and implications for ore metal transport. Geochimica et Cosmochimica
964 Acta, 61, 1017–1029.

965 Webster, J.D., and De Vivo, B. (2002) Experimental and modeled solubilities of chlorine in
966 aluminosilicate melts, consequences of magma evolution, and implications for
967 exsolution of hydrous chloride melt at Mt. Somma-Vesuvius. American Mineralogist,
968 87, 1046–1061.

969 Webster, J.D., and Holloway, J.R. (1990) and Highly Evolved Granitic Magmas.

970 Webster, J.D., Kinzler, R.J., and Mathez, E.A. (1999) Chloride and water solubility in basalt

971 and andesite melts and implications for magmatic degassing. Geochimica et
972 Cosmochimica Acta, 63, 729–738.

973 Webster, J.D., Goldoff, B., Sintoni, M.F., Shimizu, N., and De Vivo, B. (2014) C-O-H-Cl-S-
974 F volatile solubilities, partitioning, and mixing in phonolitic-trachytic melts and
975 aqueous-carbonic vapor ± saline liquid at 200MPa. Journal of Petrology, 55, 2217–2248.

976 Webster, J.D., Vetere, F., Botcharnikov, R.E., Goldoff, B., McBirney, A., and Doherty, A.L.
977 (2015) Experimental and modeled chlorine solubilities in aluminosilicate melts at 1 to
978 7000 bars and 700 to 1250 °c: Applications to magmas of Augustine Volcano, Alaska.
979 American Mineralogist, 100, 522–535.

980 Webster, J.D., Goldoff, B.A., Flesch, R.N., Nadeau, P.A., and Silbert, Z.W. (2017) Hydroxyl,
981 Cl, and F partitioning between high-silica rhyolitic melts-apatite-fluid(s) at 50-200 MPa
982 and 700-1000 °c. American Mineralogist, 102, 61–74.

983 Webster, J.D., Baker, D.R., and Aiuppa, A. (2018) Halogens in Mafic and Intermediate-Silica
984 Content Magmas. In The Role of Halogens in Terrestrial and Extraterrestrial
985 Geochemical Processes: Surface, Crust, and Mantle

986 Webster, J.D., Iveson, A.A., Rowe, M.C., and Webster, P.M. (2020) Chlorine and felsic
987 magma evolution: Modeling the behavior of an under-appreciated volatile component.
988 Geochimica et Cosmochimica Acta, 271, 248–288.

989 Zajacz, Z., Candela, P.A., Piccoli, P.M., and Sanchez-Valle, C. (2012) The partitioning of
990 sulfur and chlorine between andesite melts and magmatic volatiles and the exchange
991 coefficients of major cations. Geochimica et Cosmochimica Acta, 89, 81–101.

992

**Table 1** Experiments conducted under NNO oxygen buffer.

| Experiment number | Starting material | Pressure (MPa) | Temperature °C | $XH_2O$ (wt %) | Glass content (vol%) | Volatile mass (g) | Glass mass (g) | Duration (hours) |
|---|---|---|---|---|---|---|---|---|
| Kel14 | Basaltic andesite | 50 | 1000 | 1 | 43.9 | 0.0298 | 0.0162 | 49 |
| Kel12 | Basaltic andesite | 50 | 1050 | 1 | 47.4 | 0.0044 | 0.0446 | 36 |
| Kel9 | Basaltic andesite | 50 | 1100 | 1 | 39.5 | 0.0131 | 0.0409 | 24 |
| Kel35 | Basaltic andesite | 50 | 1050 | 0.55 | 30.1 | 0.0144 | 0.0289 | 46 |
| Kel34 | Basaltic andesite | 50 | 1025 | 1 | 36.9 | 0.0133 | 0.0433 | 42 |
| Kel23 | Basaltic andesite | 50 | 1000 | 0.56 | 28.7 | 0.0302 | 0.0211 | 48 |
| Kel2 | Basaltic andesite | 100 | 1000 | 1 | 31.0 | 0.0139 | 0.0212 | 44 |
| Kel15 | Basaltic andesite | 100 | 1100 | 1 | 43.0 | 0.0056 | 0.0448 | 24 |
| Quiz5 | Dacite | 120 | 900 | 1 | 92.1 | 0.0455 | 0.0852 | 168 |
| Quiz4 | Dacite | 120 | 800 | 1 | 86.5 | 0.0076 | 0.0798 | 170 |
| Quiz3 | Dacite | 120 | 850 | 1 | 94.6 | 0.0205 | 0.0844 | 171 |
| Quiz16 | Dacite | 120 | 900 | 0.5 | 89.0 | 0.0019 | 0.0669 | 167 |
| Quiz15 | Dacite | 120 | 800 | 0.56 | 82.4 | 0.0092 | 0.0596 | 178 |
| Quiz13 | Dacite | 120 | 850 | 0.5 | 86.6 | 0.0220 | 0.0585 | 171 |

993

Table 2: Starting conditions of matrix glass and XRF data, along with Br, Cl and F contents.

| | Quizapu | | Kelud | | |
|---|---|---|---|---|---|
| | Matrix glass | Bulk rock | Matrix glass | Bulk rock | |
| wt% | EMPA | XRF | EMPA | XRF | |
| **$SiO_2$** | 71.44 | 66.50 | 69.38 | 54.56 | |
| **$TiO_2$** | 0.34 | 0.54 | 0.53 | 0.65 | |
| **$Al_2O_3$** | 14.85 | 15.74 | 15.42 | 18.86 | |
| **FeO** | 1.59 | 2.97 | 4.00 | 8.89 | |
| **MnO** | 0.07 | 0.09 | 0.15 | 9.13 | |
| **MgO** | 0.33 | 0.87 | 1.04 | 3.73 | |
| **CaO** | 1.13 | 2.38 | 3.54 | 0.21 | |
| **$Na_2O$** | 4.39 | 5.13 | 4.26 | 0.67 | |
| **$K_2O$** | 4.02 | 3.27 | 1.74 | 2.79 | |
| **$P_2O_5$** | | 0.14 | 0.20 | 0.12 | |
| **Total** | 98.59 | 97.40 | 100.42 | 99.62 | |
| *SIMS (ppm)* | | | Sigma | | Sigma |
| F | 661 | *44* | 564 | *56* | |
| Cl | 2192 | *100* | 1476 | *14* | |
| Br | 6.1 | *0.7* | 4.3 | *0.4* | |

*Bulk rock XRF from Ruprecht et al., (2012) (Quizapu) and Cassidy et al., 2019 (Kelud).*

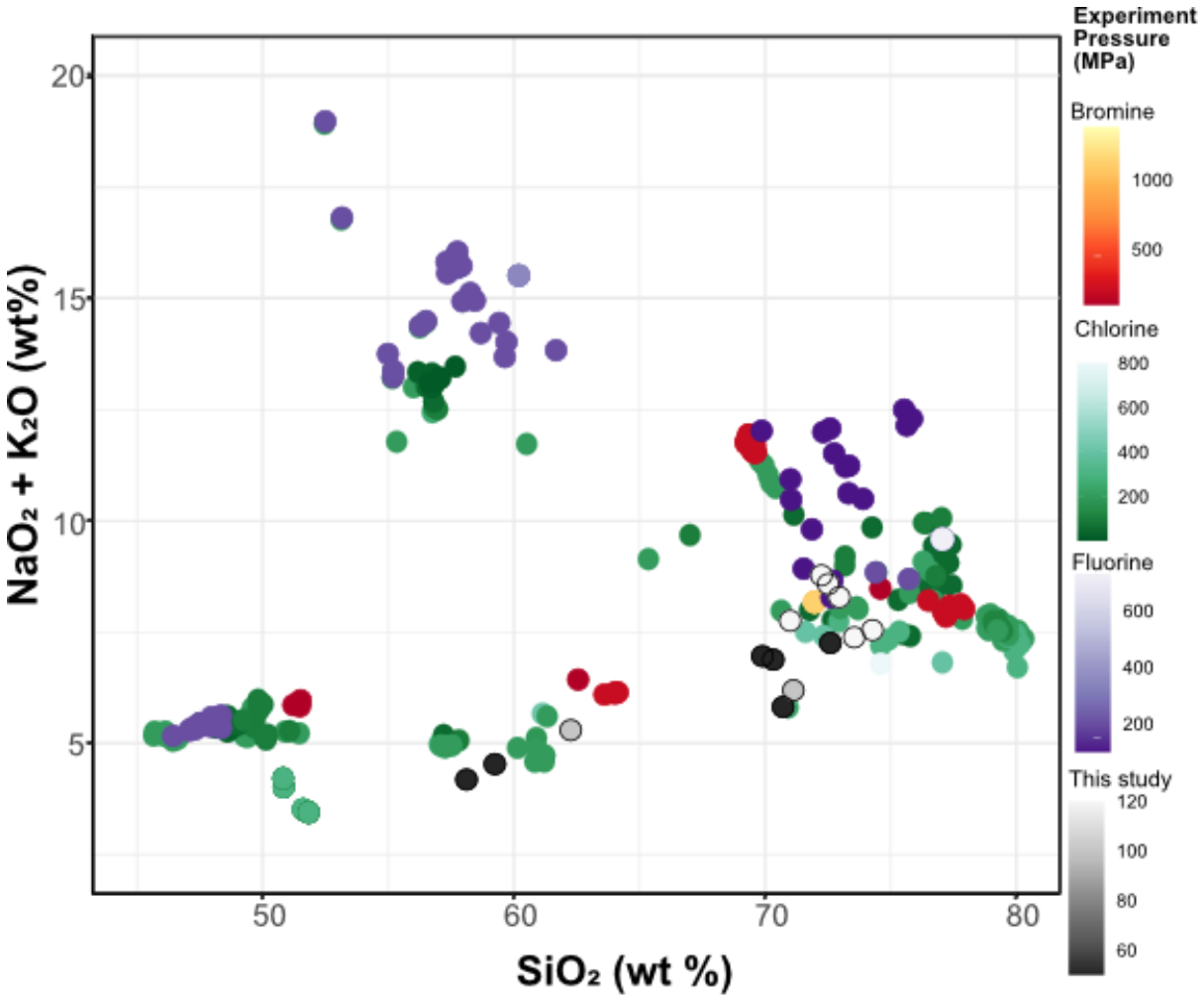


**Figure 1.** Total alkali silica plot for all the previous brine undersaturated experiments, along with their corresponding pressures (MPa), for chlorine, fluorine and bromine. The grey symbols represent the compositional space that the experiments in this study cover at pressures of 50 to 120 MPa. References for the data found in Table S1

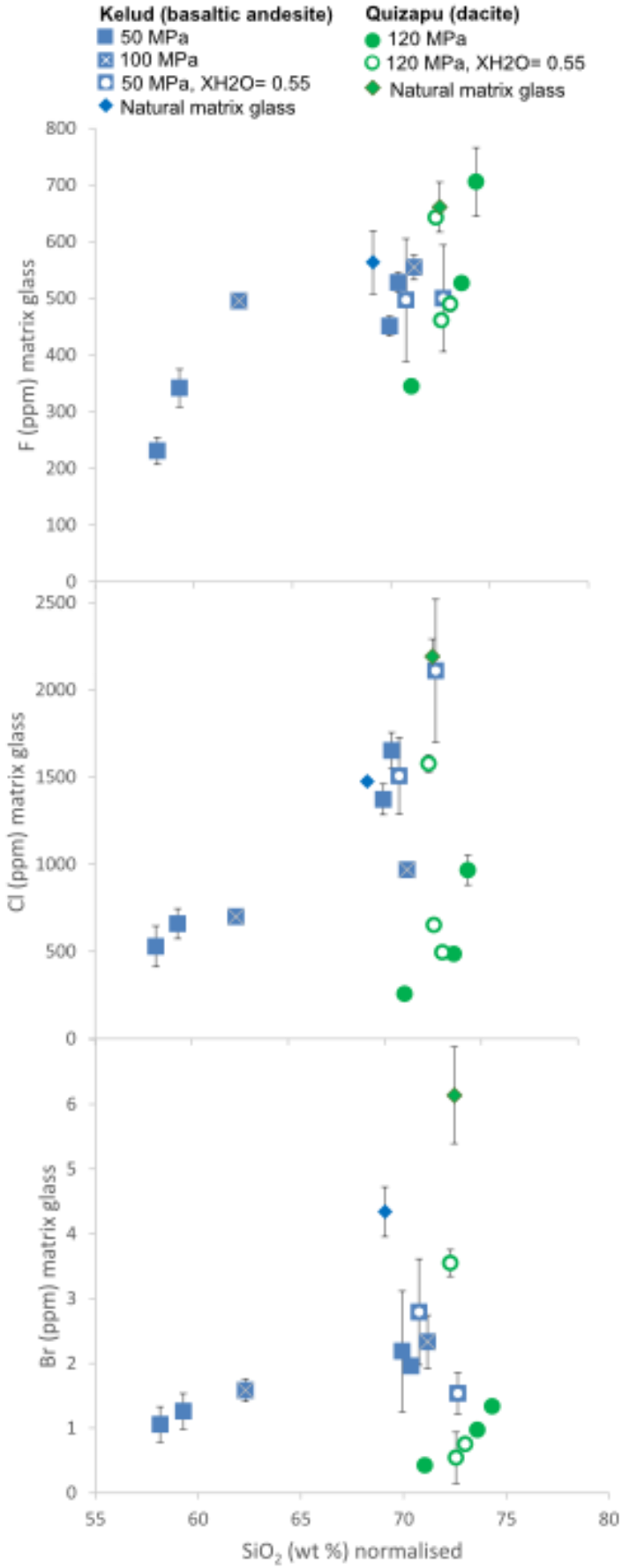


**Figure 2.** $SiO_2$ versus halogen concentrations in experimental glass products, along with their natural matrix glass compositions. Errors given are 1 standard deviation of the range of the values measured.

997

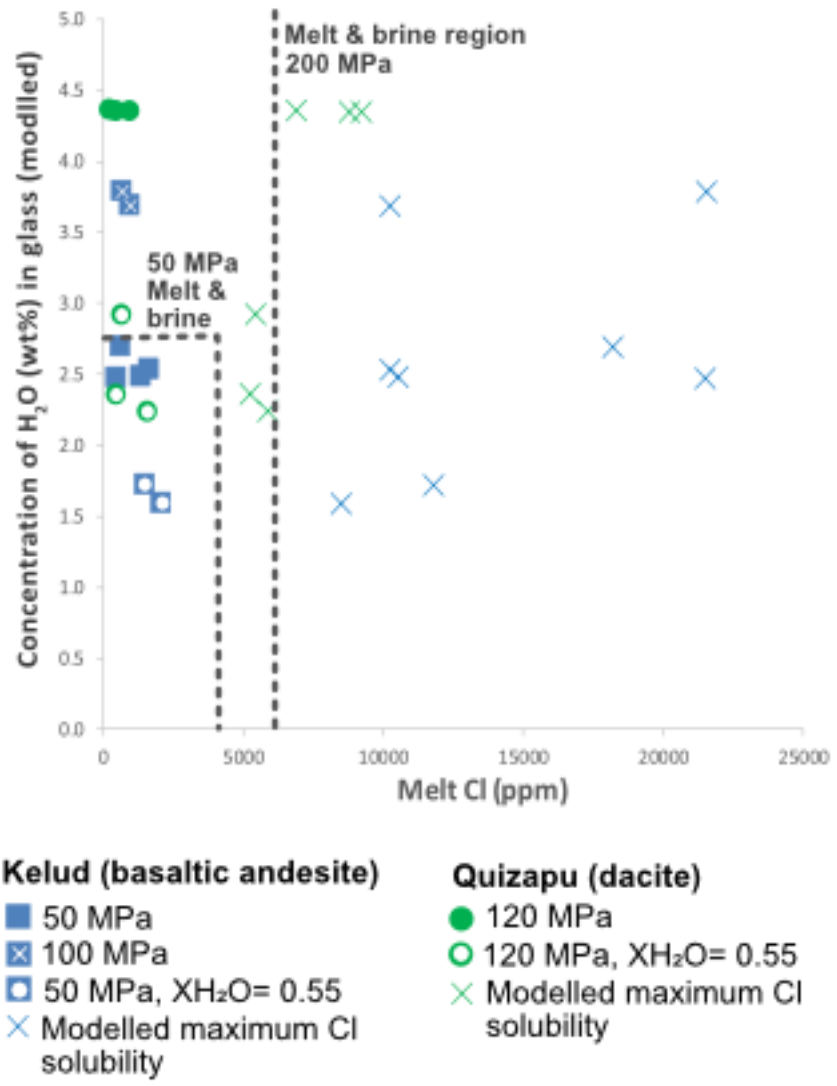


**Figure 3**. Showing Cl melt contents of the experiments of Quizapu, dacite starting material (green) and Kelud, basaltic andesite starting material (blue), with the corresponding modelled $H_2O$ contents from MELTS. The dashed lines indicate where brine and vapor phases appear at 50 MPa and 200 MPa pressures. The crosses indicate the maximum Cl contents for each experiment as modelled using Webster et al., 2015 Cl solubility model. Our experiments show brine under-saturated conditions.

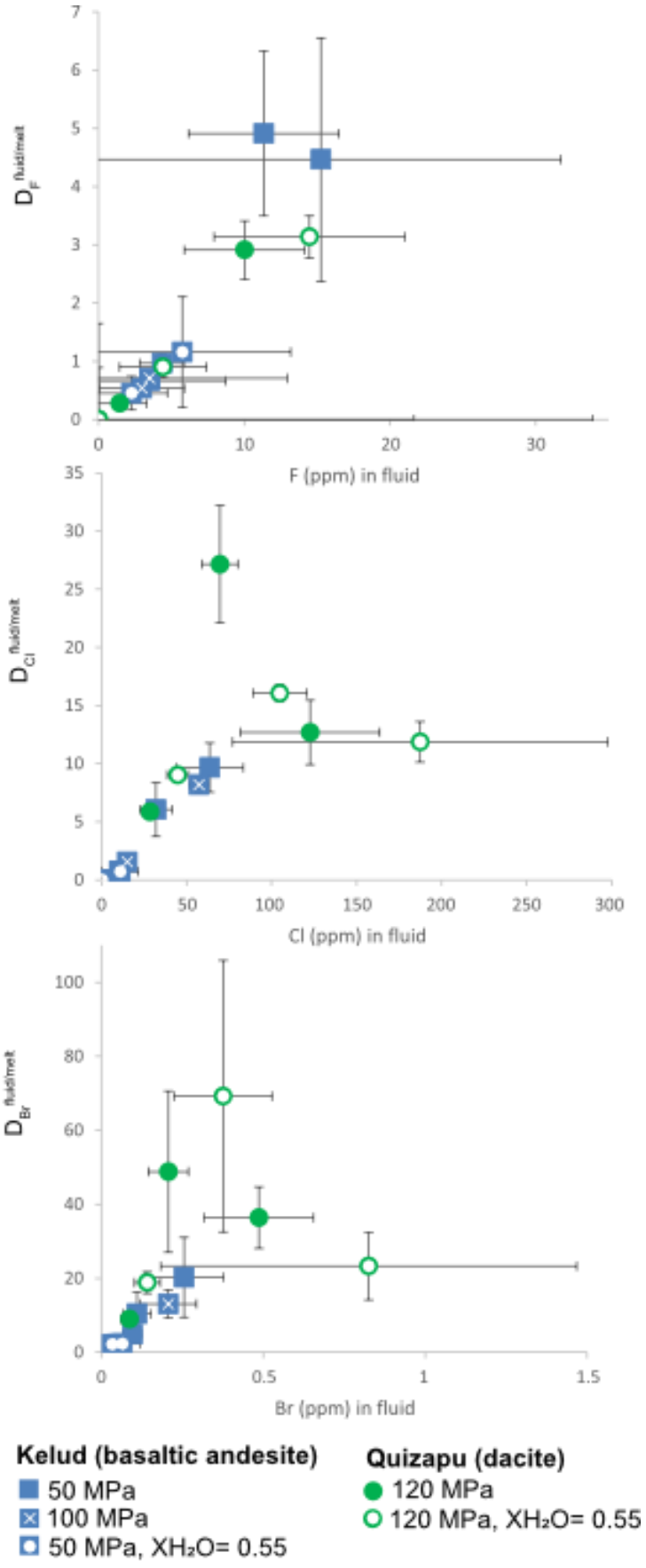


**Figure 4.** Mass balance calculated fluid halogen concentrations, against halogen fluid-melt partitioning. Maximum accumulated errors are plotted.

999

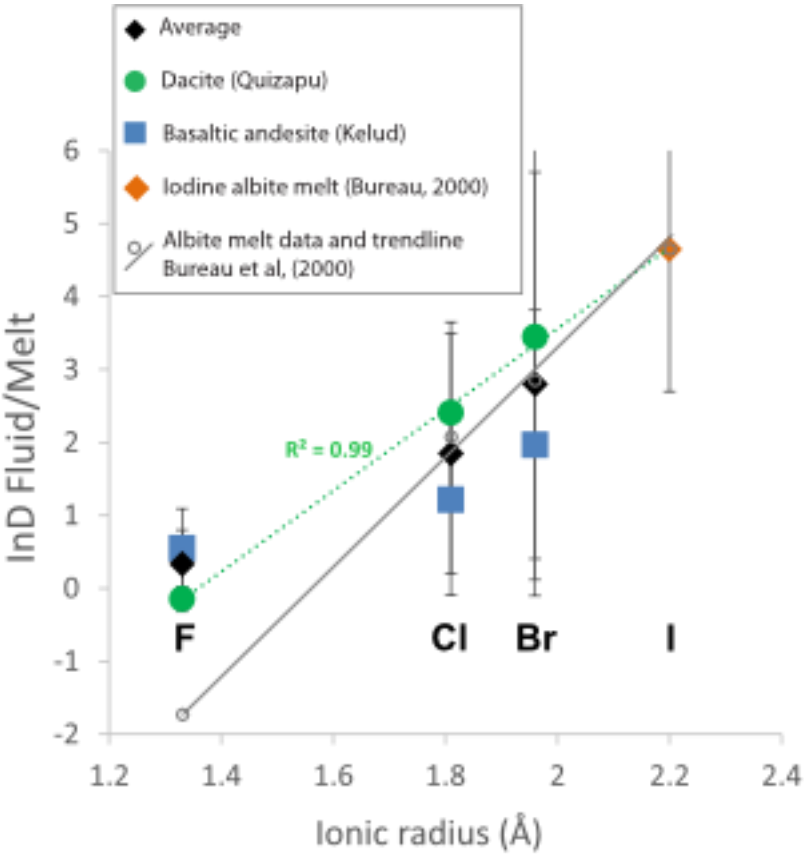


**Figure 5.** Plot of natural log of fluid/melt F, Cl and Br partitioning values in this study and iodine value from Bureau, 2000 against ionic radius in Angstroms. For comparison the dataset and trendline from Bureau et al., (2000) is plotted.The green trendline shown is from the Quizapu dataset, which represents the best correlation. Error bars indicate 1 standard deviation of the values for the pressures (50-120 MPa), temperatures (800°C – 1100°C ) and $XH_2O$ (0.55-1) conditions. The biggest difference is the differing F partitioning values (higher in this study) which alters the regression equation. The F partitioning value in Bureau et al., (2000), was from Webster et al., (1992), measured in granitic melts.

1000

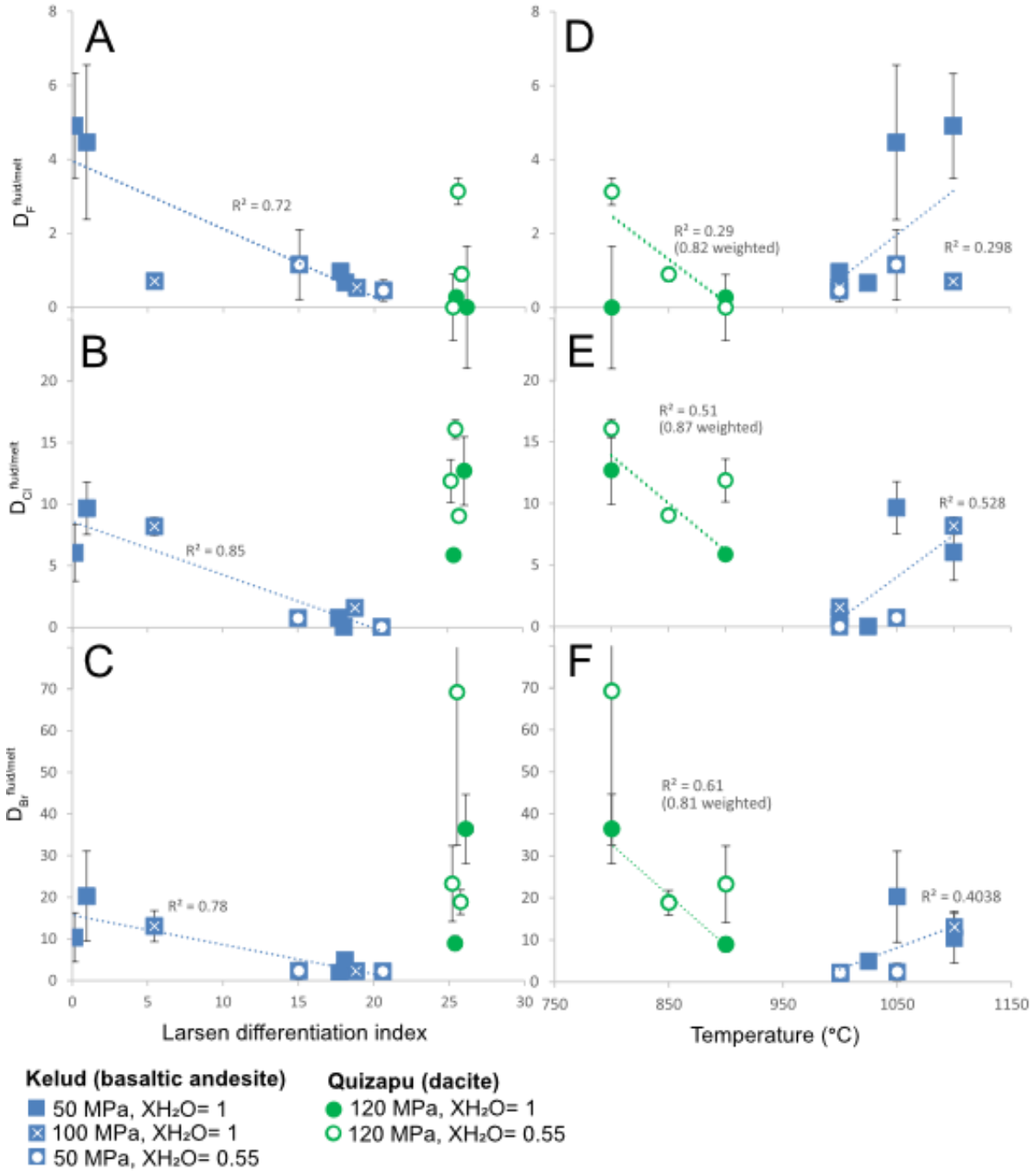


**Figure 6.** Effects of glass composition (Larsen differentiation) and temperature on bulk partitioning of halogens. $R^2$ values shown above report both the unweighted and weighted regressions. Variance-weighted regression was applied to Quizapu dataset which has higher uncertainties (D, E and F), providing revised $R^2$ values and the trend lines against temperature plotted above.

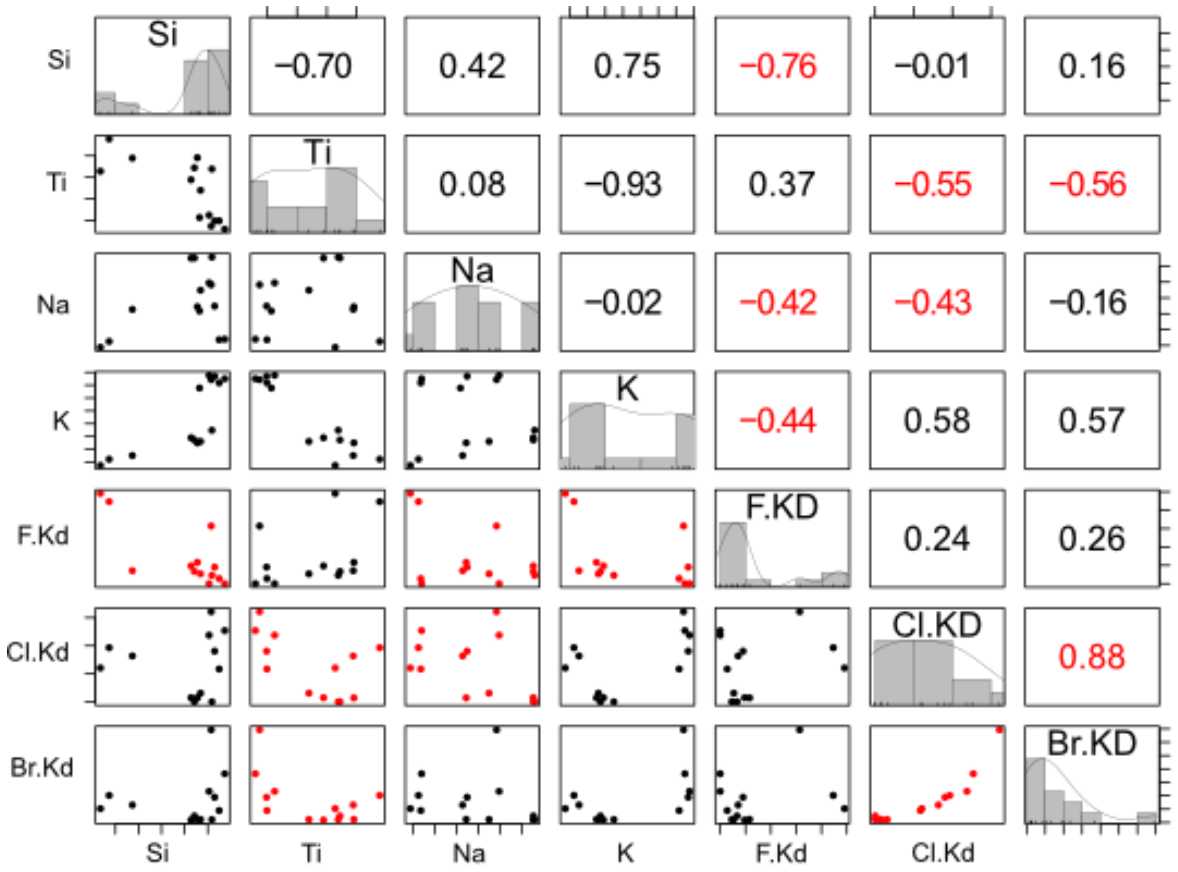


**Figure 7.** Scatter plot of matrices of different elements and the Cl, F and Br partitioning values,with bivariate scatter plots below the diagonal, histograms on the diagonal, and the Pearson correlation above the diagonal. The key correlations are highlighted in red. In the scatter plots the X axes represent the range of values of the element in the same row, while the Y axes represent the element in the vertical column.

1002

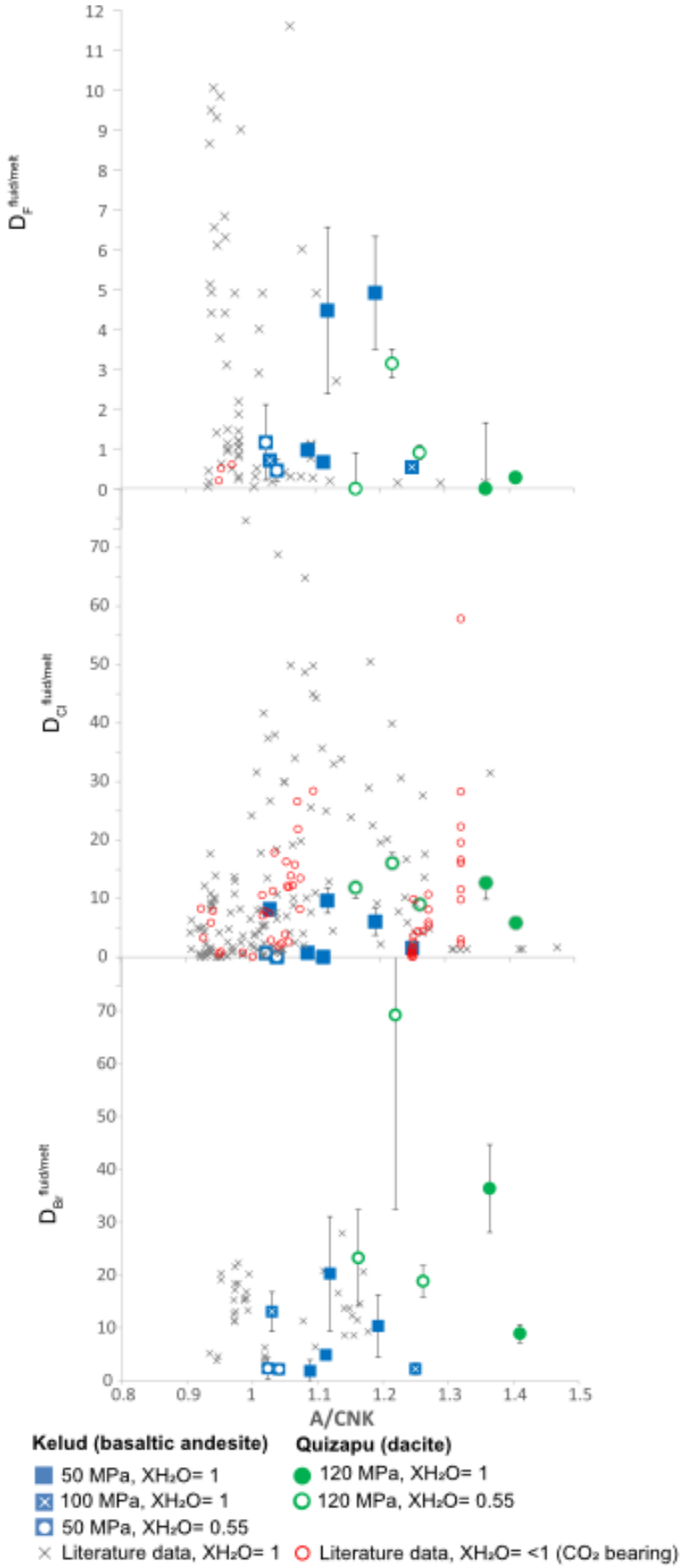


**Figure 8.** The molar Aluminium/Calcium+Sodium+Potassium ratio for data in these study as a comparison to data from literature (including $CO_2$ bearing systems) for non-brine systems, and therefore thought to represent henrian partitioning. Literature sources in table S1 and broken down by study in figure S7..

1003